Geology and geochemistry of the sediment-hosted Cheshmeh-Konan redbed-type copper deposit, NW Iran

Shahrokh Rajabpour [a,b,*], Ali Abedini [b], Samad Alipour [b], Bernd Lehmann [c], Shao-Yong Jiang [d,e]

[a] Geology Department, Faculty of Earth Sciences, Shahid Beheshti University, Tehran, Iran
[b] Geology Department, Faculty of Sciences, Urmia University, Urmia, Iran
[c] Mineral Resources, Technical University of Clausthal, 38678 Clausthal-Zellerfeld, Germany
[d] State Key Laboratory of Geological Processes and Mineral Resources, Collaborative Innovation Center for Exploration of Strategic Mineral Resources, Faculty of Earth Resources, China University of Geosciences, Wuhan 430074, China
[e] State Key Laboratory for Mineral Deposits Research, Department of Earth Sciences, Nanjing University, Nanjing 210093, China

ARTICLE INFO

ABSTRACT

The several-hundred-m-thick Miocene Upper Red Formation in northwestern Iran hosts stratiform and fault-controlled copper mineralization. Copper enrichment in the percent range occurs in dm-thick carbonaceous sandstone and shale units within the clastic redbed sequence and consists of fine-grained disseminated copper sulfides (chalcopyrite, bornite, chalcocite) and supergene alteration minerals (covellite, malachite and azurite). The copper mineralization formed after calcite cementation of the primary rock permeability. Copper sulfides occur mainly as replacement of diagenetic pyrite, which, in turn, replaced organic matter. Electron microprobe analysis on bornite, chalcocite and covellite identifies elevated silver contents in these minerals (up to 0.12, 0.72 and 1.21 wt%, respectively), whereas chalcopyrite and pyrite have only trace amounts of silver (<0.26 and 0.06 wt%, respectively). Microthermometric data on fluid inclusions in authigenic quartz and calcite indicate that the Cu mineralization is related to a diagenetic fluid of moderate-to low temperature (Th = 96–160 °C) but high salinity (25–38 wt% $CaCl_2$ equiv.). The range of $\delta^{34}S$ in pyrite is −41.9 to −16.4‰ (average −31.4‰), where framboidal pyrite shows the most negative values between −41.9 and −31.8‰, and fine-grained pyrite has relatively heavier $\delta^{34}S$ values (−29.2 to −16.4‰), consistent with a bacteriogenic derivation of the sulfur. The Cu-sulfides (chalcopyrite, bornite and chalcocite) show slightly heavier values from −14.6 to −9.0‰, and their sulfur sources may be both the precursor pyrite-S and the bacterial reduction of sulfate-bearing basinal brines. Carbonates related to the ore stage show isotopically light values of $\delta^{13}C_{V-PDB}$ from −8.2 to −5.1‰ and $\delta^{18}O_{V-PDB}$ from −10.3 to −7.2‰, indicating a mixed source of oxidation of organic carbon (ca. −20‰) and HCO_3^- from seawater/porewater (ca. 0‰). The copper mineralization is mainly controlled by organic matter content and paleopermeability (intragranular space to large fracture patterns), enhanced by feldspar and calcite dissolution. The Cheshmeh-Konan deposit can be classified as a redbed-type sediment-hosted stratiform copper (SSC) deposit.

1. Introduction

Sediment-hosted stratiform copper (SSC) deposits host major copper resources (Brown, 1984; Chartrand and Brown, 1985; Haynes, 1986; Kirkham, 1989; Hitzman et al., 2005, 2010), and are also known from the Miocene Upper Red Formation (URF) in NW Iran (Fig. 1). These deposits and occurrences are thought to

belong to a regional NW-trending belt of SSC deposits, extending for almost 170 km from Khoy in the northwest, near the Turkish-Iranian state border, to Tabriz in the southeast (Fig. 1). Only a few studies have been published previously on this copper district which had some sporadic small-scale mining in the past (Naghizadeh et al., 2008; Rajabpour et al., 2010a,b, 2013; Aghazadeh and Badrzadeh, 2011, 2012; Sadati et al., 2013, 2016). The SSC deposits and occurrences invariably occur (a) within Early to Late Miocene multiple redbed clastic sequences totaling one km or more in thickness, and (b) in the vicinity of regional faults, including the Tabriz, Mishu and Tasuj faults (Fig. 1), which controlled the evolution and structure of the Tertiary basins

* Corresponding author at: Geology Department, Faculty of Earth Sciences, Shahid Beheshti University, Tehran, Iran.
E-mail addresses: sh.rajabpour@gmail.com, sh_rajabpour@sbu.ac.ir (S. Rajabpour).

(Aghazadeh and Badrzadeh, 2011). Three major copper deposits (Ana Khaton, Sorkheh and Cheshmeh-Konan) have been mined in the past but are currently abandoned. Copper grades ranged between 2 and 4%, and silver was recovered as a byproduct, with a grade of 80–100 g/t (Aghazadeh and Badrzadeh, 2012).

The Cheshmeh-Konan copper deposit is located ~15 km NW of Tasuj County, East Azerbaijan Province, NW Iran. This deposit consists of stratiform orebodies within Miocene terrestrial clastic sediments. The copper mineralization is related to reduced gray sandstones as interlayers in the about 800-m-thick Miocene URF. Geological, geochemical, mineralogical and fluid inclusion data are presented here with the objective of elucidating the genesis of the Cheshmeh-Konan deposit.

2. Regional geological setting

Southwestern Iran is characterized by the collision of the Arabian Plate and the Central Iranian block along the NW-SE trending Zagros fold-and-thrust belt (Nowroozi, 1971; Berberian and King, 1981). The orogenic process is reflected in the late Kimmeridgian compressional phase, related to the subduction of the High Zagros Alpine Ocean, and probably continues until recent time (Nowroozi, 1971). The final closure of the High Zagros Alpine Ocean was related to the Late Cretaceous Laramide phase, which involved regional greenschist metamorphism, magmatism, and extensive folding and uplift (Berberian and King, 1981; Berberian, 1983). The extensive Eocene volcanic and plutonic activity of Central Iran, with major porphyry Cu deposits in the Urmia-Dokhtar volcanic belt, is related to subduction and collision along the Zagros Thrust (Dewey et al., 1973; Foster, 1976; Jung et al., 1976; Brookfield, 1977; Farhoudi, 1978). The post-collisional convergence of the Arabian and Asian plates resulted in progressive folding, faulting, and gradual rise of the mountain belts which established the present-day physiographic features of NW Iran (Berberian and King, 1981). During the Middle and Late Alpine orogenic movements, folding and uplift of the mountain belts continued, followed by subsidence in the central part of the zone (Berberian and King, 1981; Berberian, 1983). As a result of these movements, most parts of NW Iran became land with inter-mountain basins. The URF is one of the most important Cenozoic clastic units to which components were supplied from the rising mountains and deposited in the inter-mountain fault-bounded subsiding basins (Fig. 1).

Because of frequent fluctuations of sea-level in Miocene time, successions of thick lithologic units of calcareous and evaporitic rocks were deposited in the inter-mountain sedimentary basins in northwestern Iran. The continental redbeds overlie the Miocene sedimentary sequence. The formation of thick salt (halite) beds in the area indicates ingress of ocean waters into narrow continental rift zones. The marine sedimentary basins were initially developed in early Eocene and lasted up to middle Miocene (Rahimpour-Bonab et al., 2007). The change of the depositional environment of the Tabriz-Khoy Basin from marine to non-marine, generated transitional successions of marine, marginal-marine, and continental sediments. The evaporitic units display textures testifying to a shallow lagoonal environment. The evaporites have high bromine contents reflecting derivation from lagoonal brines occasionally mixed with meteoric waters (Rahimpour-Bonab et al., 2007). The Cheshmeh-Konan area is located near the boundary between the Alborz Block and the Tabriz-Khoy Basin, which is outlined by the regional-scale Tasuj and Tabriz Faults (Figs. 1 and 2).

3. Geology of the Cheshmeh-Konan area

The Cheshmeh-Konan geological map and its stratigraphic units are shown in Figs. 2 and 3. In the Cheshmeh-Konan area, the base-

ment rocks below the URF are very poorly exposed, with only a few outcrops adjacent to the Tasuj Fault, presumably Early Permian in age (Khodabandeh and Aminifazl, 1993). However, granitic rocks of Permian-Triassic age constitute the predominant clast lithology in the overlying Miocene conglomerates (Khodabandeh and Aminifazl, 1993). The Cretaceous sequence is disconnected from the overlying Miocene sequences by a minor syn-rift stratigraphic discontinuity (Fig. 2). On top of the discontinuity are the Lower Miocene redbeds of the URF, reaching up to ~800 m in thickness in the study area. Miocene rocks with a total thickness of probably more than 2000 m comprise of red conglomeratic and very coarse-grained sandstone, generally decreasing in grain size upward in the succession. The clasts of these rocks are polymictic, poorly sorted and show a low degree of roundness. Textural and geochemical properties suggest intermediate (andesitic to dacitic) to basic volcanic rocks (dissected arc) as parent rocks. According to Amini (1997), Amini and Anketell (2015), the detrital components of the URF basin were mainly derived from the Eocene volcaniclastic-dominated Karaj Formation, as well as the Oligo-Miocene Qom Formation (QF) and the Lower-Miocene Lower Red Formation (LRF) (Fig. 1a). The results are in agreement with sedimentological characteristics that indicate their short transportation history and high deposition rate in a tectonically active setting with arid to semi-arid climate (Amini, 1997; Rajabpour et al., 2010a).

The URF consists mostly of coarse-grained, poorly sorted, red arkoses, generally showing cross-bedding. The base and the top of the URF are marked, respectively, by (a) M1: conglomerate beds containing volcanic fragments alternating red to gray siltstone and sandstone with variegated pure salt rocks, (b) M2: gray to tan-colored sandstone, micro-conglomerate, shale and gypsum, and (c) M3: brown sandstone with conglomerate intercalations, gypsum and very thin salt beds (Rahimpour-Bonab and Kalantarzadeh, 2005). Copper mineralization occurs at the top of the URF, in fine-grained gray sandstone, a few meters below the transitional contact with the overlying Late Miocene sediments (M^{12} and M^{st} Formation) and Pliocene volcanic rocks (PlQ^d Formation; Fig. 3). At the Cheshmeh-Konan village, numerous reduced (gray) sandstone layers with indications of Cu mineralization are exposed. Folding and faulting in the northern and southern Mishu hills along the Tabriz Fault has distorted the pattern of mineralized layers, particularly in the northern part of the Mishu hills (Fig. 1 B).

4. Geological characteristics of the Cheshmeh-Konan copper deposit

In the Cheshmeh-Konan area, the Cu mineralization is hosted as interlayers in the URF, which is in tectonic contact with the Early Miocene sequence (Figs. 2 and 3). The strata dip ~35° to the north. These layers are fine-grained sandstones, enriched in secondary copper minerals, and interbedded with decimeter- to centimeter-thick carbonaceous silty layers. The tectonic surveys of the Cheshmeh-Konan area indicate the existence of several faults which have deformed the exposed sequence (Khodabandeh and Aminifazl, 1993; Rajabpour et al., 2013). The geological map of the Cheshmeh-Konan deposit with lines of exploration trenches and location of samples for chemical analysis is shown in Fig. 4. The Cheshmeh-Konan mineralization occurs as several successive decimeter-thick, concordant, copper-mineralized, fine- to coarse-grained clastic layers with high organic matter content (Fig. 5a, b). Bleaching of sedimentary rocks related to the oxidation of sulfides and formation of iron oxides/hydroxides is a common feature (Fig. 5c). The mineralized interval represents fining-upward cycles, including intermittent decimeter- to meter-thick graybeds of conglomerate, sandstone and siltstone (Rajabpour et al., 2013).
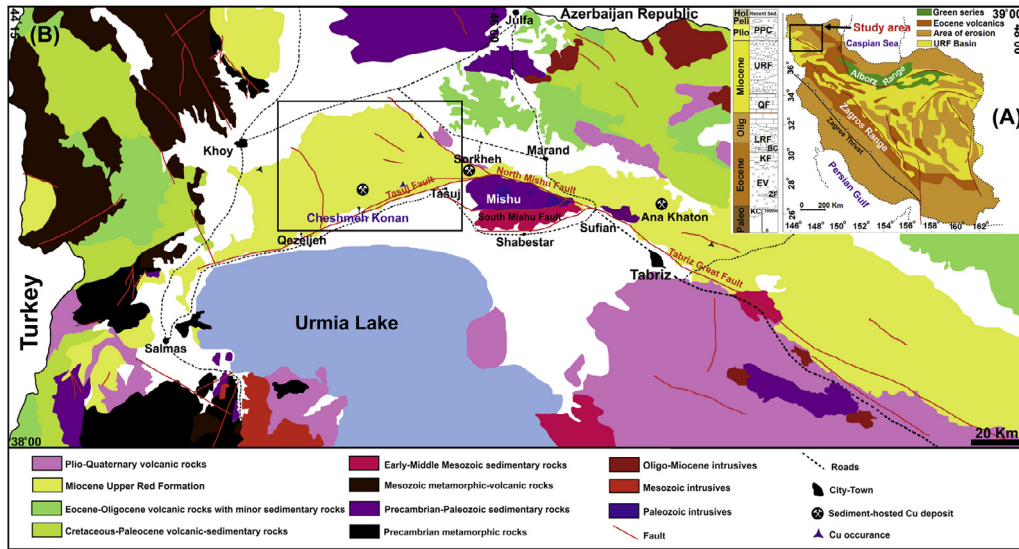
Fig. 1. (a) Paleogeography of the URF basin in Iran (modified from GSI, 1999; Berberian and King, 1981) and the simplified Cenozoic stratigraphic column of the Central Zone. KC = Kerman Conglomerate, EV = Eocene volcanics, ZF = Ziarat Formation, KF = Kond Formation, BC = Basal Conglomerate, LRF = Lower Red Formation, QF = Qom Formation, URF = Upper Red Formation, PPC = Plio-Pleistocene Conglomerate; (b) Geological map of northwestern Iran and location of the studied area (modified after Ghorashi and Arshadi, 1978; Aghazadeh et al., 2015). (For interpretation of the references to color in this figure legend, the reader is referred to the web version of this article.)
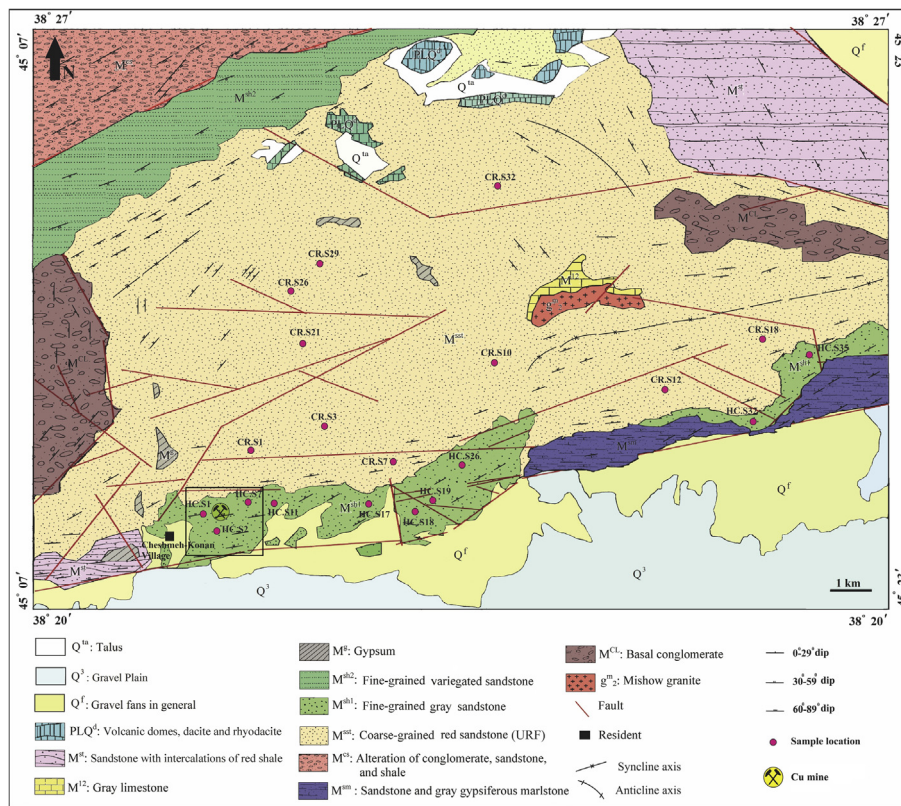
Fig. 2. Geological map and location of the sediment-hosted Cheshmeh-Konan copper deposit within Miocene red beds, northwestern Iran (modified after Khodabandeh and Aminifazl, 1993). (For interpretation of the references to color in this figure legend, the reader is referred to the web version of this article.)

The copper mineralization at the surface mainly turned to supergene malachite and azurite, giving a remarkable blue-green color to the mineralized horizons (Fig. 5d). The deposit is well exposed by short exploration trenches and shafts. Twenty-five mineralized layers, 5–200 cm in thickness extend laterally for at least 300 m (Fig. 5d). They are fine-grained cupriferous sandstones that occur within graybeds. The copper mineralization is always associated with organic matter as sheet-like bodies with extensive horizontal dimensions, following stratigraphic surfaces (Fig. 5d, e). In the studied area, bleached sandstones host fossil wood mineralized with malachite and chalcocite (Fig. 5e). Shale and marlstone units also host mineralized layers within the sequence (Fig. 5f).

The footwall redbeds are composed of coarse-grained reddish clastic sediments, and the graybeds are represented by the overly-
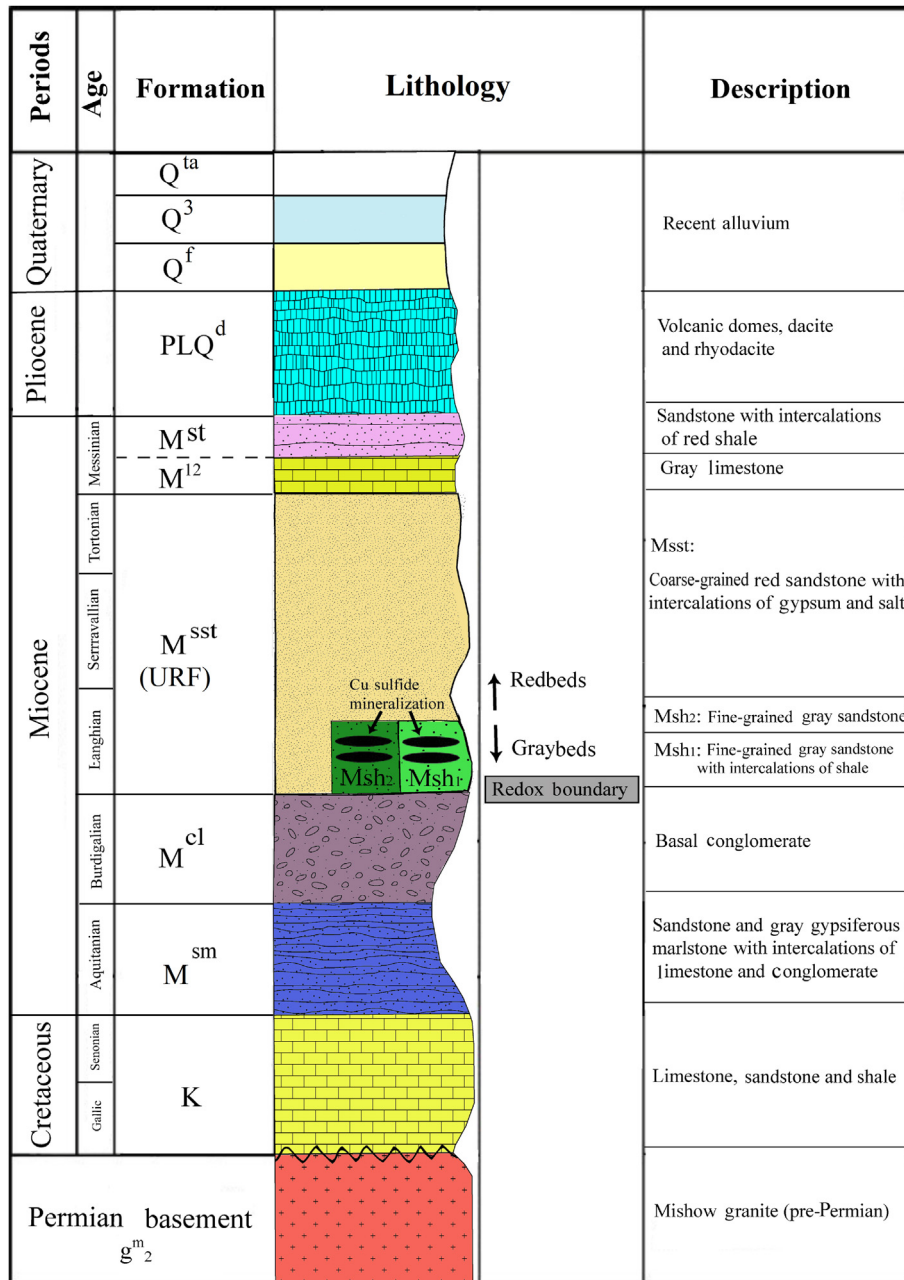
Fig. 3. Stratigraphic column for the Cheshmeh-Konan property including copper mineralization, showing the general redox boundary between portions of graybeds (M^{sh1} and M^{sh2} units) and redbeds (M^{sst} unit: URF).

ing fine- to medium-grained gray sandstones. The sandstones consist of quartz, plagioclase, K-feldspar, augite, hornblende, mica, and chert and lithic fragments. These components are cemented by sparry carbonate (calcite and dolomite) (3–5%), iron oxides (2–3%) and clays (3–10%). Angular clastic to sub-rounded quartz grains with a grain size of 0.3–0.5 mm on average are the main minerals (42–60%) in the sandstones. Accessory components (modal contents < 1%) are detrital biotite, muscovite, chlorite, zircon and rutile. The detrital grains are cemented by quartz and minor calcite. In addition, late ferric hydroxides grain-coating cement occurs at the unmineralized footwall series, reddening them. The microscopy study indicates that the amount of feldspar (plagioclase, albite and orthoclase) is high, approximately 30%. Some of the sandstones are moderately well sorted and have good maturity, which according to Folk's (1980) classification are litharenite, sublitharenite and subarkose (Fig. 6).

According to petrographical observation, the sandstones have calcitic and dolomitic cements (Fig. 7a) and feldspar is replaced by coarse-grained dolomite within sublitharenitic sandstone, and the anhedral fine-grained dolomite replaced by quartz and chalcopyrite. In Fig. 7b, the hematite pigmentation is pre-diagenetic (detrital) and authigenic hematite (the reddish tint in Fig. 7b) is due to diagenetic Fe-oxyhydroxides. The diagenetic reddening suggests the former presence of oxidized fluids (probably brines) which are required for leaching and transport of copper (Boyle et al., 1989; Brown, 2009). Malachite seams in fractured detrital quartz are common (Fig. 7c).

Petrographic studies are conducted on the various facies of the URF, its interbedded gray sandstones and sulfide ores in order to distinguish the timing of ore-stage sulfide formation within the geological evolution of the Cheshmeh-Konan host rocks: (1) sedimentation, (2) diagenesis/mineralization, (3) tectonic deforma-
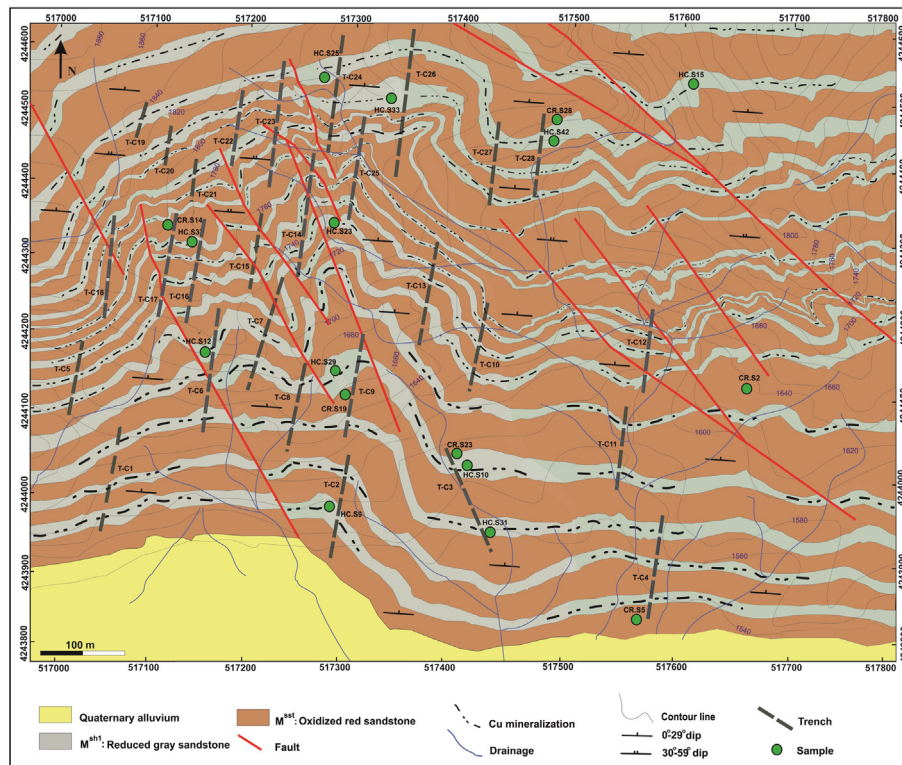
Fig. 4. Geological map of the Cheshmeh-Konan copper deposit with exploratory trench lines for Cu-mineralization zones and sample location. Plan view of the map showing the ore zone patterns as described in the text and in Fig. 2.

tion/overprinting, and (4) supergene oxidation. A hand-specimen of the chalcocite and malachite mineralization around organic matter within subarkosic sandstone is shown in Fig. 7d. The type of organic matter in the mineralized sandstone is detrital plant debris. Fossilized wood debris is abundant in the Cheshmeh-Konan deposit (Fig. 7e). Petrographic study shows that the plant debris has retained its original cellular structures and is replaced by sulfides. BSE microphotographs indicate rectangular- (Fig. 7f) and lenticular-like (Fig. 7g) fossilized wood cellular structures.

A detailed description of various sulfides in the Cheshmeh-Konan deposit is as follows

4.1. Pyrite, a pre-ore sulfide

Microscopic studies show that two major types of pyrite occur: framboidal, and fine-grained diagenetic pyrite (Figs. 7h, i and 8a, b), although coarse-grained pyrite is also visible but it is not the dominant textural type. The framboidal pyrite commonly occur as aggregates of pyrite grains (Fig. 7h, i; commonly 25 μm, and up to 1 mm or more). The fine-grained pyrite mostly occurs as dissemination (Fig. 8a, b, generally up to 15 μm). Unoxidized parts of gray sandstones are characterized by disseminated fine-grained pyrite. Under the microscopic, the fine-grained pyrite is observed in a close association with organic matter, suggesting reduced conditions and bacterial sulfate reduction. In addition to the framboidal texture, the fine-grained pyrite may form in the intergranular pore spaces as nodules (smaller than 1 cm). Both the framboidal and fine-grained pyrites are considered to be originally syndiagenetic, having formed in the earliest unconsolidated sandstones associated with organic matter (Fig. 9).

4.2. Primary ore-stage cupriferous sulfides

The major mineralization stage of the Cheshmeh-Konan area is characterized by disseminated cupriferous sulfides. The primary

copper sulfides formed dominantly as cement within gray sandstones. Sulfide minerals are rarely detectable with naked eye.

(1). **Chalcopyrite**: remnants of fine-grained pyrite may still be associated with chalcopyrite mineralization. Disseminated anhedral grains and aggregates of chalcopyrite occur after fine-grained pyrite (Fig. 8b–d). Chalcopyrite at microscopic scale is commonly coarser than other sulfide minerals (greater than 0.25–0.5 mm) and primarily is seen within pores of reduced sandstone (Fig. 8b, c). Chalcopyrite in the vicinity of organic matter is seen as lamellae, so that in some of the samples there are large veinlets (Fig. 8b). Subsequently, chalcopyrite is replaced by the more Cu-rich sulfides (e.g., bornite and chalcocite; Fig. 8e–g).

(2). **Bornite**: occurs as irregular disseminated grains, replacing chalcopyrite or pyrite. It may form pseudomorphs after very fine-grained euhedral pyrite or occupy primary intergranular and secondary diagenetic porosities of the sediments. Bornite commonly shows aggregates with up to 800 μm in diameter. It also exhibits a basket-weave intergrowth with chalcopyrite lamellae (Fig. 8e). The most common sulfides associated with bornite are chalcocite and chalcopyrite, with which bornite forms boundary contacts (Fig. 8f, g).

(3). **Chalcocite I**: commonly occurs as dissemination and filling primary intergranular porosities. Chalcocite I is irregular in shape and shows a variable size from 200 μm to more than 0.5 mm (Fig. 8g). It is also observed as rims around the parageneticaly earlier sulfides such as chalcopyrite and bornite, but it is not seen as inclusions in those sulfides. Chalcocite is often associated with bornite (Fig. 8g) and, less commonly with chalcopyrite. Abundant fossilized wood debris with well-preserved wood cell texture in the reduced host sandstone is mineralized by ore-stage sulfides in interstitial spaces between cells (Fig. 8h, i).
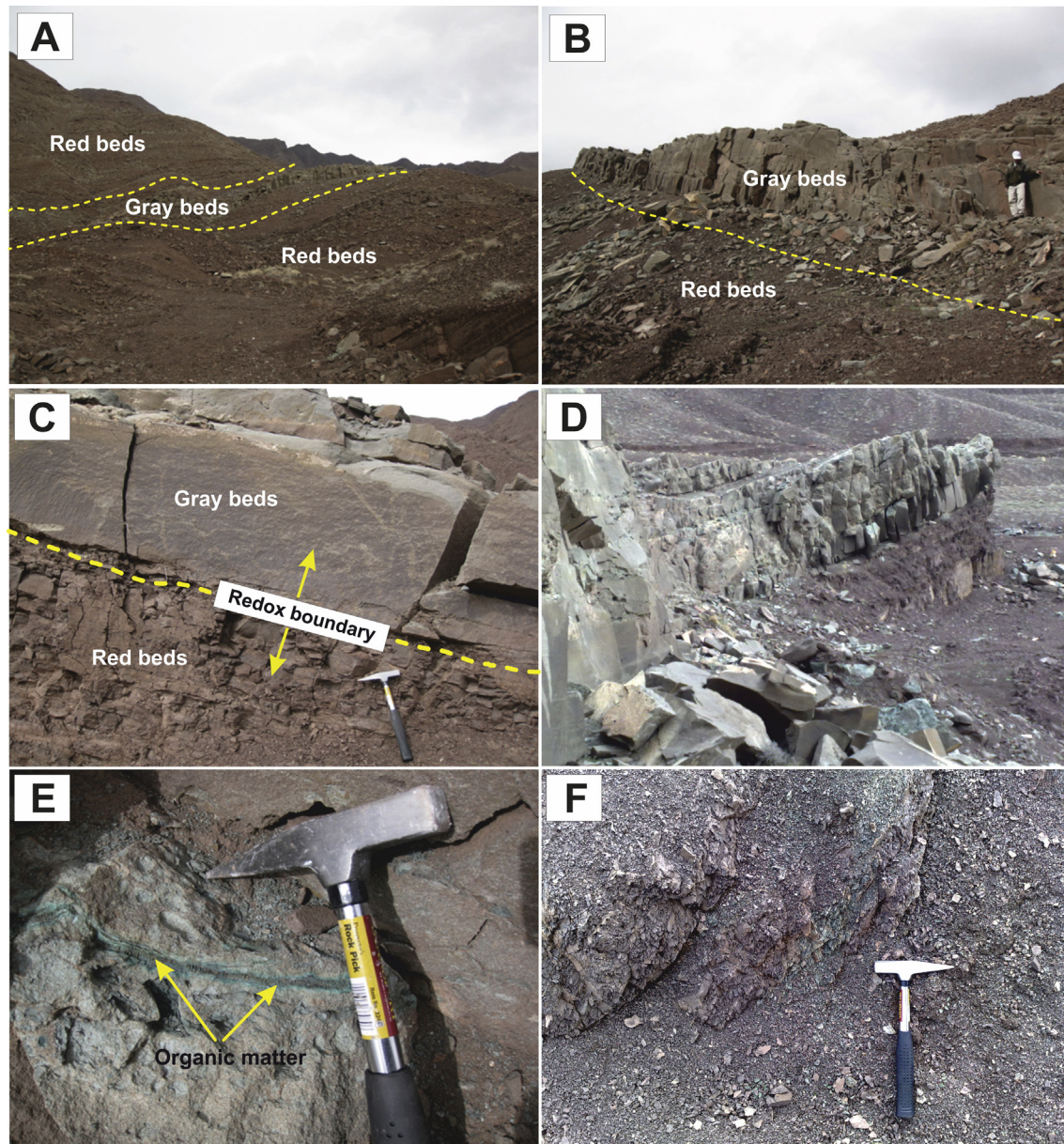
Fig. 5. (a) Field photographs of the boundary of stratigraphic unmineralized red bed units and gray sandstone (graybeds) or copper-rich mineralization M^{sh1} unit in the Cheshmeh-Konan deposit; (b) The boundary of stratigraphic unmineralized red bed and gray sandstone in the M^{sh2} unit; (c) The separation of stratigraphic oxidized-unmineralized red bed; reduced gray sandstone in the M^{sh1} unit and redox boundary between two layers; (d) The mineralized fine-grained gray sandstone; (e) Accumulation of the organic matter in the gray sandstones host fossil wood remains mineralized with malachite and chalcocite; (f) Shale and marl unit. (For interpretation of the references to color in this figure legend, the reader is referred to the web version of this article.)

4.3. Post-ore mineralogical features

Post-ore events include advanced burial diagenesis, tectonic overprint such as late fracturing of the host rocks, and also supergene alteration (Fig. 9). Post-ore tectonic deformation had an important role in the Cheshmeh-Konan deposit (Fig. 9). Field observation indicates that the reduced gray sandstone strata and their sediment-hosted mineralization are folded, tilted, and faulted, and consequently the lateral continuity of the mineralization has been disrupted severely. Supergene alteration occurs in the uppermost 2 meters of the exposed orebodies with malachite as the major mineral (Fig. 7c, d) and goethite staining on the mineralized outcrops. Other supergene minerals include chalcocite II, covellite and azurite, iron oxy-hydroxides (e.g., limonite) and ferric oxide (hematite). Both malachite and, to a lesser extent, azurite occur as rims over chalcocite, bornite, and chalcopyrite, and they may also fill dissolution cavities in sandstones. The formation of ore-stage minerals apparently terminated after a silicification event because this alteration effectively eliminated the porosity and permeability of the host sandstones.

5. Samples and analytical methods

A variety of analytical techniques were employed on selected samples to evaluate different parameters as follows. Seventy rock samples were collected from the URF and mineralized sandstone outcrops and also exploratory trenches in the area (Figs. 2 and 4). Sixty-five samples (Tables 1–3) were analyzed by X-ray fluorescence spectrometry at the Geological Survey of Iran for major elements to characterize the bulk rock composition. Twenty samples
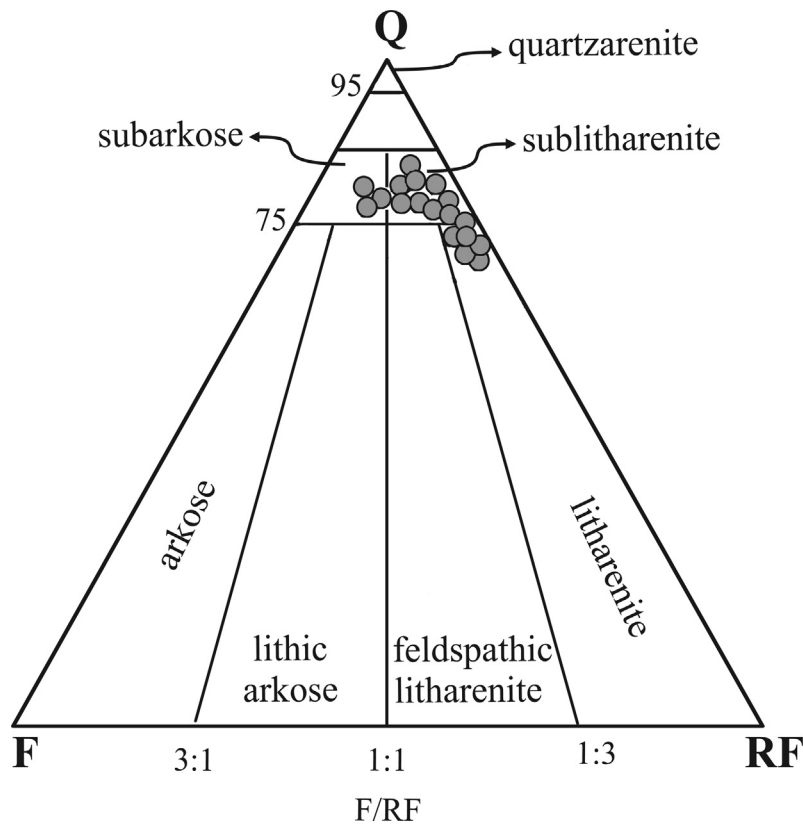
Fig. 6. Mineralogical classification of the Cheshmeh-Konan sandstones (Folk, 1980).

for trace elements (Tables 1 and 2) were measured at SGS Analytical Services (Vancouver, Canada) by inductively coupled plasma mass spectrometry (ICP-MS). Two lines of sample digestion were used: (1) Method ME-MS81 (refractory elements) with fusion at 1000 °C of 0.2 g sample powder and 0.9 g of lithium metaborate flux, and subsequent dissolution in 100 mL of 4% HNO_3/2% HCl solution; (2) Method ME-MS61 (base metals) with four-acid (perchloric, nitric, hydrochloric and hydrofluoric acid) digestion of 0.25 g of sample powder and subsequent dissolution with hydrochloric acid.

Chemical analyses and back-scattered electron images were made of selected grains of ore minerals using the electron microprobe; these data were employed to confirm optical identification of minerals, assist in evaluating textural relationships used to establish the paragenetic sequence, and assess mineral chemistry, particularly within phases that exhibit a close relationship. Electron microprobe analyses were performed at the China University of Geosciences (Wuhan), using a JXA-8100 electron microprobe. After preliminary energy-dispersive X-ray (EDX) analysis and detailed examination of 15 samples in back-scatter electron mode (BSE), we selected the most typical samples for more detailed study. A set of 18 elements (Se, As, Ge, S, Pb, Bi, Sb, Sn, Fe, Co, Te, Ag, Cd, Zn, Cu, Ni, Au and Mn) was chosen for spot analysis of mineral grains (Tables 4–6). Operating conditions were 20 kV accelerating voltage, a beam current of 20 nA, and a beam diameter of 5 μm. Counting times ranged from 20 to 60 s, a dwell time of 30 s on peak, and a 30-s off-peak background on either side of the peak. A combination of natural and synthetic standards was used to calibrate the instrument. Standard substances refer to GB/T 15074-2008 general rules for EPMA analysis.

A fluid inclusion study was undertaken to assess the evolution of the ore-forming fluids in the paragenetic sequence and to evaluate physico-chemical controls on ore mineral deposition. Double-polished thick sections (100–150 μm thick) were prepared from selected samples in which the mineral paragenesis had been established. Microthermometric analyses were conducted on a subset of the thick sections to investigate the fluid chemistry and evaluate the temperature conditions of ore deposition. Suitable fluid inclusions for the microthermometric study were found in quartz and calcite in the veinlets of mineralized samples (Table 7). Fluid inclusion data were obtained from seven sections, with a Linkam THMSG-600 heating-freezing stage. Fluid inclusions with suspected leakage (very heterogeneous bubble/liquid ratio) were avoided. Salinities were calculated assuming a H_2O-$CaCl_2$ system (Crawford, 1981) because in the fluid inclusions the salts are not NaCl and KCl but probably $CaCl_2$ in composition as we will demonstrate in a later section.

Stable isotope analyses were conducted on selected samples of vein minerals to constrain the source of the ore-forming fluids and sulfur in the deposits. Oxygen and carbon isotope analyses obtained from calcite separates were used to identify the probable origin of the ore-forming fluids and to evaluate the possibility of physico-chemical controls of fluids. Carbon and oxygen isotope analyses of carbonates were carried out at the Institute of Geology and Geophysics, Chinese Academy of Sciences (IGGCAS), Beijing, on ten carbonate-cemented mineralized sandstone samples. Using microdrilling techniques, carbonate cements with different textures were separated (Table 8). The samples were analyzed using a Finnegan–MAT Delta plus mass spectrometer. Precision of the analyses (1σ) was estimated to be better than ±0.2 per mil according to standard analyses. Isotope values are reported in standard delta notation as per mil difference from the V-PDB standard. Sulfur isotope analyses of sulfide minerals were used to assess the source of sulfur. The sulfur isotopic composition of the samples was analyzed by in situ laser combustion from standard polished sections (Table 8). An area with 300–400-μm diameter of the sul-
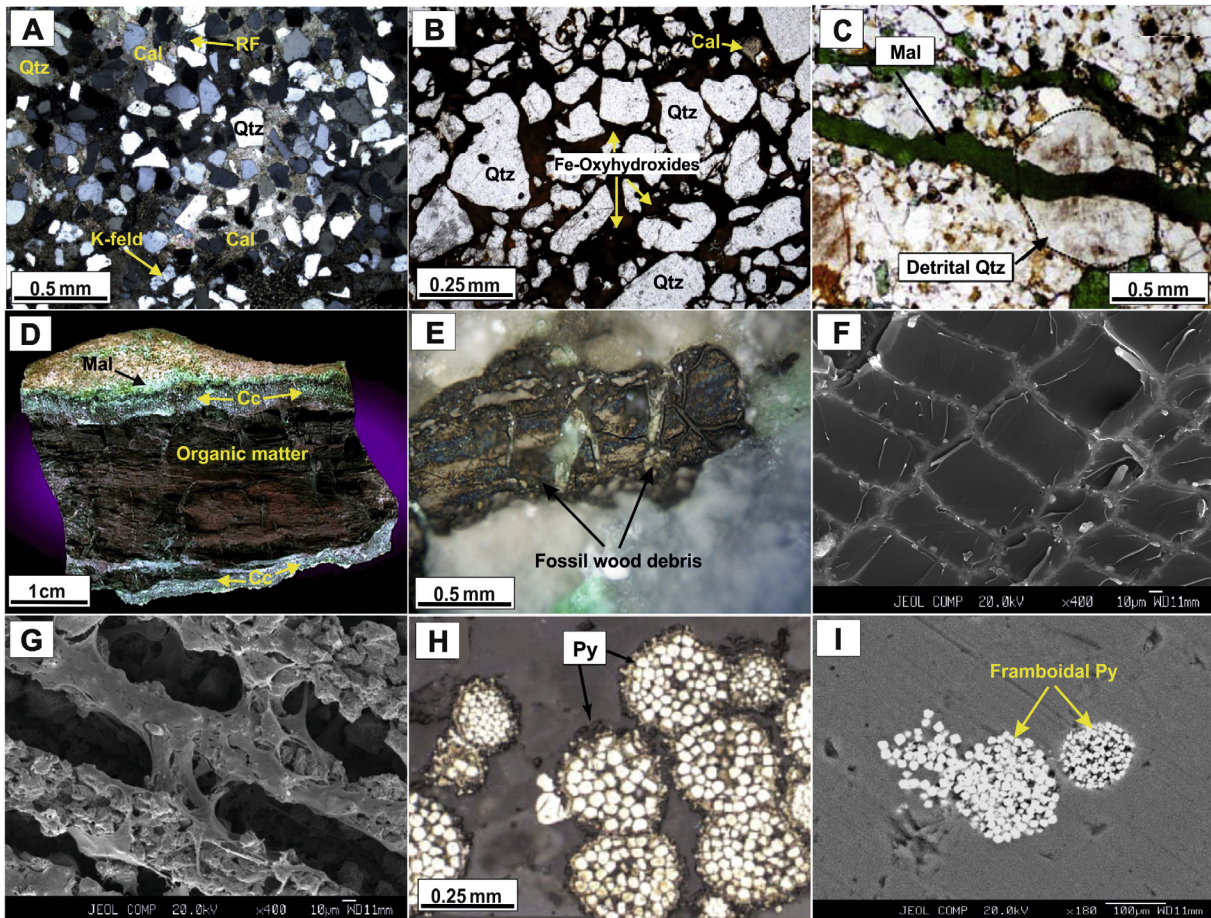
Fig. 7. (a and b) Coarse-grained sublitharenitic sandstones with calcitic and dolomitic cement (the reddish tint in photomicrograph b is due to Fe-oxyhydroxides; transmitted, plane-polarized light); (c) Fractures within detrital quartz that is filled by malachite (transmitted, plane-polarized light); (d) A hand-specimen of the chalcocite and malachite mineralization within subarkosic sandstone including organic matter as fossil wood debris; (e) Fossil wood debris; reflected, plane-polarized light; (f) Backscattered electronic photomicrograph (BSE) of rectangular fossilized wood cellular structures; (g) BSE photomicrograph of lenticular fossilized wood cellular structures; (h) Framboidal pyrites (reflected, plane polarized light); (i) BSE photomicrograph of framboidal pyrite; Abbreviations: Cal: calcite; Cc: chalcocite; K-feld: potassium feldspar; Mal: malachite; Py: pyrite; Qtz: quartz; RF: rock fragment.

fide mineral was combusted using a Spectron Lasers 902Q CW Nd-YAG laser, in the presence of excess oxygen (Fallick et al., 1992). The released SO_2 gas was purified in a vacuum line, which operates similar to a conventional sulfur extraction line (Kelley and Fallick, 1990). The sulfur isotopic composition of the purified SO_2 gas was measured using a VG SIRA II gas mass spectrometer. The reference gas in the mass spectrometer was calibrated by running a suite of international and lab standards. The analytical precision (1σ) was about ±0.1 per mil. Sulfur isotope compositions are reported in standard per mil (‰) relative to the Vienna Canyon Diablo Troilite (V-CDT).

6. Results

6.1. Major and trace element composition of bulk rocks

Bulk rock chemical data of the barren URF and mineralized sandstones are listed in Tables 1–3. The contents of SiO_2 (46.9–52.1 wt%), Al_2O_3 (9.24–12.6 wt%), K_2O (1.07–2.41 wt%), Na_2O (1.1–2.9 wt%) and CaO (8.6–11.5 wt%) are within the ranges expected for litharenite, sublitharenite and subarkose. The diagrams of log (SiO_2/Al_2O_3) *vs.* log (Na_2O/K_2O) (Pettijohn et al., 1972; Fig. 10a) and log (SiO_2/Al_2O_3) *vs.* log (Fe_2O_3/K_2O) (Herron, 1988; Fig. 10b) show the chemical classification of the Cheshmeh-Konan sandstone samples as litharenite, sublitharenite

and subarkose, which are in good agreement with the petrographical observations. The negative correlation between Al_2O_3 and K_2O (r = −0.32) indicates that K-feldspar increases as quartz decreases. The positive correlation between Al_2O_3 and SiO_2 (r = +0.4) suggests that these oxides are mostly controlled by feldspars and, to a lesser extent, by diagenetic illite. Major elements for the copper-mineralized sandstones generally vary within the same ranges observed for the unmineralized sandstones, but they show high copper contents between 0.8 and 6.7 wt% Cu.

6.2. Electron probe micro-analysis (EPMA) data

EPMA data for pre-ore, ore-stage and post-ore stage sulfide minerals are listed in Tables 4–6, respectively.

6.2.1. Pre-ore stage sulfides

The microprobe analyses of individual pyrite grains are predominantly lower than the expected stoichiometric proportions, with Fe = 45.0 ± 1.0 wt% and S = 52.7 ± 0.6 wt% (n = 17). The data show that the two types of pyrite have different copper concentrations. Copper can be accommodated within the pyrite structure in significant amounts as submicroscopic inclusions of Cu-sulfides (e.g., chalcopyrite, bornite and chalcocite), which in some cases may reach percent levels (Einaudi, 1968; Huston et al., 1995; Pacevski et al., 2008; Reich et al., 2013). EPMA results for fram-
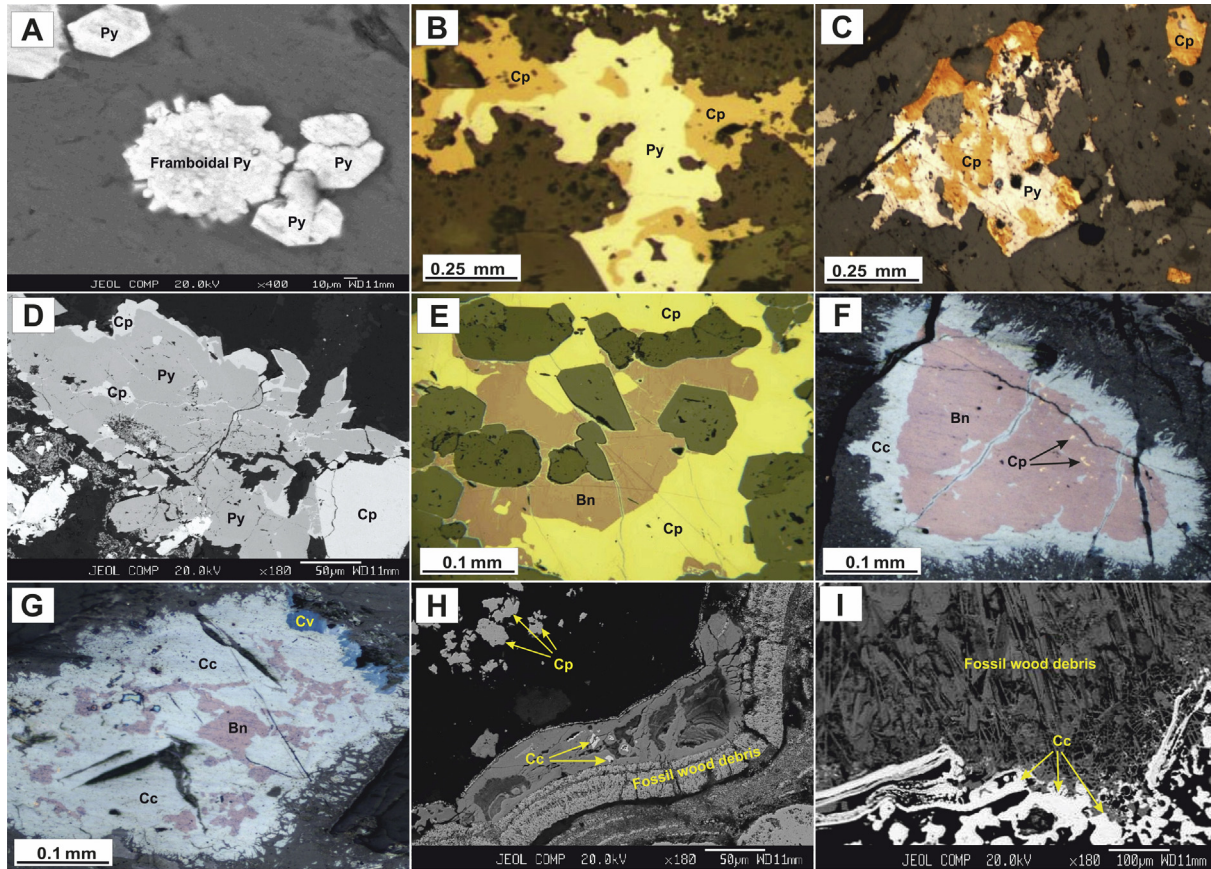
Fig. 8. (a) BSE photomicrograph of framboidal pyrite and aggregation of fine-grained pyrite; (b and c) The overgrowth pyrite and chalcopyrite mineralization within subarkosic sandstone (reflected, plane-polarized light); (d) BSE photomicrograph of the occurrence of euhedral pyrite replaced by chalcopyrite; (e) Replacement of chalcopyrite by bornite within subarkosic sandstone (reflected, plane-polarized light); (f) BSE photomicrograph of the occurrence of enriched copper sulfides (i.e. bornite, chalcocite and covellite) replaced in chalcopyrite with impregnation texture; (g) Replacement of chalcopyrite and bornite by chalcocite and covellite (reflected, plane-polarized light); (h and i) BSE photomicrographs of chalcopyrite and chalcocite mineralization in fossilized wood cells. Abbreviations: Bn: bornite; Cc: chalcocite; Cp: chalcopyrite; Cv: covellite; Py: pyrite.

boidal pyrite range from 0.05 to 0.67 wt% Cu (mean of 0.27 ± 0.67 wt% Cu; n = 8) and for fine-grained pyrite from 0.67 to 3.31 wt% Cu (mean of 1.97 ± 1.19 wt% Cu; n = 9), respectively. This indicates that the copper content in pyrite increases significantly from the framboidal pyrite to the fine-grained pyrite. The framboidal pyrite shows an average Ag content of 0.05 wt%, Pb content of 0.17 wt%, and Co content of 0.07 wt%. In contrast, the fine-grained pyrite shows higher contents of Ag (0.09 wt%), Pb (0.46 wt%) and Co (0.14 wt%). But the concentrations of Cd and Ni are lower in the fine-grained pyrites (Table 4). Most pyrite samples are As-poor and also have Se values below the limit of detection (LOD).

6.2.2. Primary ore-stage sulfides (chalcopyrite, bornite and chalcocite I)

EPMA results for chalcopyrite, bornite and chalcocite I are shown in Table 5. Chalcopyrite hosts lower amounts of detectable trace elements relative to bornite and chalcocite I. Among twenty-six grains analyzed, Ag content increases from chalcopyrite (mean 0.02 ± 0.01 wt%; n = 12) through bornite (mean 0.06 ± 0.03 wt%; n = 8) to chalcocite I (mean 0.36 ± 0.27 wt%; n = 6). The Zn concentrations gradually increase and can reach up to 0.11 wt%. The copper phases have relatively high Pb contents (0.01–0.59 wt%), possibly present as submicroscopic PbS inclusions in these phases. Bismuth, Co, Ge, Ni, Se and Te are at or below the analytical detection limit. Gold and As concentrations are also low; some micro-

probe analysis had no detectable Au or As, and others had detectable but low levels (Table 5).

6.2.3. Post-ore supergene enrichment stage sulfides

EPMA data of chalcocite II and covellite are listed in Table 6. These results indicate that the Ag content in the Cu-rich sulfides of the post-ore supergene enrichment stage is relatively high and increases from chalcocite II (0.27 ± 0.18 wt%; n = 9) to covellite (0.40 ± 0.36 wt%; n = 8). All other trace components (As, Au, Bi, Cd, Co, Fe, Ge, Mn, Ni, Pb, Sb, Se, Sn, Te, Zn) in both chalcocite II and covellite are at or below the detection limit (Table 6).

6.3. Fluid inclusion microthermometry

Fluid inclusions were studied in quartz and calcite samples from veinlets and cements related to the ore-stage in the mineralized sandstones of the Cheshmeh-Konan copper deposit. Fluid inclusions mostly occur homogeneously distributed, classified petrographically as primary in origin using the criteria of Roedder (1984). Fluid inclusions showing evidence of post-entrapment modifications, such as necking down, were avoided for microthermometric measurements. Primary fluid inclusions have regular morphology and small size, usually between 4 and 10 μm in the longest dimension, and are aqueous two-phase liquid-vapor (L + V), with ~6 vol% of bubble at room temperature (Fig. 11). These inclusions homogenize to a liquid phase and do not contain recognizable CO_2 or CH_4. Homogenization temperatures (Th) and ice-

Paragenetic stage / Minerals & events	Pre-ore stage	Main-ore stage	Post-ore stage		
	Syn. Diagenesis	Early Diagenesis	Advanced Diagenesis	Tectonic Overprinting	Supergene Alteration
Reddening (Iron oxide)	▬▬▬	▬▬▬			
Micrite	▬				
Organic matter destruction	▬▬▬▬▬▬▬▬▬▬▬▬▬▬▬▬▬				
Dissolution & porosity generation		▬▬▬	▬		
Compaction		▬			
Early fracturing			▬		
Calcite recrystallization			▬		
Late fracturing				▬	
Calcite cement I	▬				
Dolomitization	▬				
Framboidal pyrite	▬▬				
Disseminatd pyrite	▬▬▬▬				
Chalcopyrite		▬▬▬			
Bornite		▬▬			
Chalcocite I		▬▬			
Calcite cement II		▬			
Silica			▬		
Calcite cement III				▬	
Chalcocite II					▬
Covellite					▬
Malachite					▬
Azurite					▬
Hematite					▬
Goethite					▬

Fig. 9. Paragenetic sequence of minerals and associated events in the Cheshmeh-Konan deposit.

Table 1
Bulk-rock chemical composition (major and trace elements) of selected unmineralized sandstone samples of the Miocene URF (see Fig. 2 for sample location).

Sample No.	CR.S1	CR.S3	CR.S7	CR.S10	CR.S12	CR.S18	CR.S21	CR.S26	CR.S29	CR.S32
SiO_2 (wt%)	47.5	51.1	50.4	51.2	49.6	51.5	50.1	52	47.7	48.4
Al_2O_3	10.1	11.3	10.2	10.4	9.6	11.4	10.7	9.7	9.82	11.2
Fe_2O_3	5.6	6.4	5.59	5.7	6.3	5.4	6.7	5.7	5.9	6.24
CaO	11.4	8.99	9.89	8.6	10.1	9.5	10.4	10.6	9.84	11.2
Na_2O	1.7	2.1	1.9	2.1	1.8	2.3	1.3	1.92	2.4	1.65
MgO	6.25	5.97	7.12	6.4	5.83	5.92	6.24	6.74	6.7	6.44
K_2O	1.53	1.21	1.37	1.47	1.36	1.42	1.36	1.37	1.34	1.53
TiO_2	0.72	1.37	0.69	0.74	0.85	1.42	1.38	0.87	1.44	0.63
Cr_2O_3	0.06	0.31	0.08	0.17	0.06	0.05	0.14	0.08	0.18	0.24
MnO	0.1	0.11	0.1	0.1	0.09	0.1	0.08	0.09	0.1	0.12
P_2O_5	0.15	0.12	0.13	0.12	0.32	0.31	0.18	0.14	0.22	0.18
L.O.I.	13.3	10.9	11.9	12.6	13.1	10.7	11.4	10.2	12.4	10.7
Total	98.4	99.8	99.3	99.6	99.0	100.0	100.0	99.4	98.0	98.5
U (ppm)	2.09	2.15	1.41	2.42	2.31	1.82	2.16	1.4	2.25	1.53
Th	5.2	5.8	4.4	3.7	4.8	5.1	4.6	4.3	5.8	4.2
Ba	150	490	170	162	470	174	160	480	170	300
Cu	31	48	44	32	46	43	41	38	34	44
Ag	2	1	2	2	2	1	2	1	1	3
Hf	3	10	4	3	4	7	4	3	6	7
Co	29.3	27.1	29.6	18.6	14.9	15.7	18.9	19.2	19.4	24.6
Pb	23	17	14	15	21	17	19	27	31	25
Zn	54	64	76	56	51	54	61	42	52	61
Nb	13	21	11	11	14	16	12	18	16	11
Cs	1.6	0.7	1.4	1.2	0.7	0.6	0.8	0.4	0.6	1.3
Rb	43.6	30.8	38.8	37.7	35.2	34	34.1	41.4	33.8	36.4
V	102	168	105	96	110	126	87	112	137	125
Y	21.6	21.5	19.6	21.5	20.2	19.2	20.6	20.5	19.7	21.2
Zr	120	420	130	240	130	120	120	360	130	260
Ni	201	227	220	206	225	266	245	267	268	214

Table 2
Bulk-rock chemical composition (major and trace elements) of selected mineralized samples from the Cheshmeh-Konan copper deposit (see Fig. 2 for sample location).

Sample No.	HC.S1	HC.S2	HC.S7	HC.S11	HC.S17	HC.S18	HC.S19	HC.S26	HC.S32	HC.S35
SiO_2 (wt%)	49.7	50.9	52.1	51.8	49.2	51	50.3	46.9	50.4	49
Al_2O_3	10.3	10.3	9.55	9.64	10.6	9.75	10.7	12.6	9.8	9.62
Fe_2O_3	2.97	2.92	2.6	2.85	2.82	2.51	2.94	3.7	2.74	2.7
CaO	9.38	10.3	11.5	9.8	10.6	10	9.75	10	11.2	9.4
Na_2O	2.1	2.2	2.3	2.1	2.3	2.2	2.3	2.3	2.1	2.1
MgO	5.38	5.25	3.92	4.52	5.32	4.48	5.93	4.77	4.85	5.1
K_2O	1.47	1.4	1.51	1.44	1.58	1.62	1.34	1.43	1.52	1.38
TiO_2	0.48	0.45	0.39	0.65	0.58	0.36	0.78	0.77	0.64	0.52
Cr_2O_3	0.1	0.07	0.04	0.07	0.06	0.05	0.12	0.06	0.04	0.08
MnO	0.09	0.09	0.1	0.08	0.12	0.11	0.1	0.08	0.1	0.12
P_2O_5	0.38	0.18	0.18	0.27	0.14	0.29	0.1	0.23	0.25	0.27
L.O.I	12.4	13.1	12.6	12.3	12.6	12.4	12.1	12.5	12.9	12.3
Total	94.7	97.1	96.8	95.5	95.9	94.7	96.4	95.3	96.5	92.5
U (ppm)	2.29	2.46	1.87	3.56	4.2	4.96	1.61	2.96	2.54	2.18
Th	3.8	3.8	3.2	4.1	3.6	3.1	4.2	5.2	4.7	4.1
Ba	940	550	320	750	862	300	180	1400	520	480
Cu (%)	2.8	3.9	4.2	2.6	3.1	3.2	5.9	4.3	3.7	5.6
Ag	34	44	48	29	34	45	51	48	38	47
Hf	3	3	2	2	3	2	4	3	3	4
Co	19.5	16.9	14.8	17.2	16.7	15.9	24.6	17.7	18.4	15.8
Pb	23	28	36	28	33	29	32	36	29	52
Zn	43	52	57	49	52	51	68	48	41	52
Nb	9	9	8	11	9	7	13	18	12	11
Cs	0.7	0.9	0.5	0.8	0.7	0.7	1	0.8	0.6	0.7
Rb	33.6	32.7	35.3	35.6	34.7	36.7	35.8	32	33.5	34.1
V	108	97	84	94	1.2	86	120	124	116	89
Y	14.2	14.2	14.5	15.6	14.7	14.2	17.5	16.2	14.4	15.3
Zr	90	90	80	110	90	70	140	130	120	120
Ni	216	213	177	182	179	176	216	198	212	213

melting temperatures (Tmi) were obtained on 150 fluid inclusions (Table 7). During heating, homogenization to the liquid phase occurs in a range from 125 to 160 °C (average 145 °C; n = 97) for quartz and from 96 to 139 °C (average 119 °C; n = 53) for calcite (Fig. 11). Eutectic temperatures were close to −49 °C, indicating that other salts than NaCl and KCl occur in the solution, probably $CaCl_2$ (Crawford, 1981; Davis et al., 1990). Temperatures of ice melting (Tm$_{ice}$) range between −41 and −25 °C and correspond to a salinity range of 25–38 wt% $CaCl_2$ equiv. (average 31 wt% $CaCl_2$ equiv.) for quartz and vary from −36.5 and −34 °C, corresponding to a salinity range of 31–33 wt% $CaCl_2$ equiv. (average 32 wt% $CaCl_2$ equiv.) for calcite (Table 7).

6.4. Stable isotope analyses

6.4.1. Carbon and oxygen isotopes
Carbon and oxygen isotope analyses were performed on calcite and dolomite. The results are listed in Table 8 and shown in Fig. 12. The $\delta^{13}C$ $_{V-PDB}$ data of calcite show a negative range between −8.2 and −5.1‰ (average −6.7‰; n = 10), and the $\delta^{18}O$ $_{V-PDB}$ data range from −10.3 to −7.2‰ (average −8.9‰; n = 10). The $\delta^{13}C$ $_{V-PDB}$ versus $\delta^{18}O$ $_{V-PDB}$ plot of bulk calcite and dolomite cements shows a positive correlation for calcite and dolomite cements (Fig. 12).

6.4.2. Sulfur isotopes
The results of sulfur isotope analyses are listed in Table 8 and shown in Fig. 13. The pyrite, chalcopyrite, bornite and chalcocite in the mineralized sandstones all show negative $\delta^{34}S_{V-CDT}$ values from −41.9 to −9.0‰. The $\delta^{34}S$ values for pyrite samples range between −41.9‰ and −16.4‰ (average −31.4‰), where the framboidal pyrite shows the most negative values between −41.9 and −31.8‰ (n = 3; Fig. 13), and the fine-grained pyrite has relatively heavier $\delta^{34}S$ values (−29.2 to −16.4‰; n = 3; Fig. 13). Values for chalcopyrite, bornite and chalcocite are slightly heavier, ranging from −12.0 to −9.0‰ (average −10.8‰), −13.1 to −10.4‰ (average −11.8‰) and −14.6 to −12.6‰ (average −13.6‰), respec-

tively. No significant difference exists between the $\delta^{34}S$ values of the copper sulfides (Table 8).

7. Discussion

7.1. Ore-forming process

Epigenetic overprint by copper-bearing fluids during diagenesis and replacement of earlier formed pyrite and organic matter has emerged as the most probable environment of ore formation in SSC deposits (Brown, 1971, 1984; Chartrand and Brown, 1985; Haynes, 1986; Kirkham, 1989; Branam and Ripley, 1990). At all levels of sulfide occurrences, the host strata are more reduced (graybeds) than the surrounding more oxidized redbeds. In fact, copper sulfides occur as replacement of pyrite which had previously replaced or filled cells of organic matter, as well as replacing calcite cement and detrital calcite grains, strongly supporting the introduction of mineralizing fluids during diagenesis of the sandstone hosts. In general, the configuration of the mineralized zone and its position immediately adjacent to a stratigraphically defined redox boundary, together with replacement textures, indicate an overprint of copper-bearing fluids on originally pyritic graybeds.

According to our data, the earliest sulfides (framboidal pyrite, fine-grained pyrite, chalcopyrite, bornite) were deposited before the lithification of the host rocks, i.e. they are syndiagenetic in origin. This interpretation is based on the supposition that early diagenetic processes start when sedimentation is ongoing. Framboidal pyrite can be formed directly from the seawater or from the pore water as a syn-diagenetic mineral (Berner, 1970, 1984) with sulfur supplied from bacterial reduction of seawater sulfate (Becking et al., 1960; Annels, 1974; Sweeney et al., 1986). As already noted, the diagenetic model postulates that copper sulfide minerals formed by the replacement of pre-ore reactants (organic matter, diagenetic pyrite, and cements) by copper-rich solutions. Besides of sulfate-reducing bacteria, the formation of syn-diagenetic pyrite requires three components: sulfate, bacteriologically metaboliz-

Table 3
Bulk-rock chemical composition (wt%) of selected unmineralized and mineralized samples from the Cheshmeh-Konan copper deposit (See Fig. 4 for sample location).

Sample No.	SiO₂	Al₂O₃	Fe₂O₃	CaO	Na₂O	MgO	K₂O	TiO₂	Cr₂O₃	CuO	MnO	P₂O₅	LOI	Total
CR.S2	50.3	9.8	6.4	9.22	2.3	6.48	1.24	1.38	0.08	0.04	0.10	0.37	11.4	99.1
CR.S5	51.6	10.1	5.27	8.62	2.1	6.25	1.47	1.2	0.09	0.03	0.09	0.28	12.2	99.3
CR.S14	50.8	10.2	5.59	9.38	2.2	7.12	1.4	0.76	0.04	0.05	0.08	0.16	12.6	100.3
CR.S19	51.8	9.68	4.6	10.5	2.3	6.25	1.6	0.56	0.24	0.06	0.10	0.17	11.9	99.7
CR.S23	51.2	9.24	6.1	10.8	1.8	5.97	1.61	0.36	0.04	0.05	0.11	0.24	11.7	99.2
CR.S28	49.5	10.2	6.35	9.75	2.3	6.72	1.37	0.84	0.10	0.20	0.10	0.12	12.3	99.8
HC.S9	50.9	11.3	3.7	10.2	2.3	4.7	1.42	0.39	0.11	0.60	0.08	0.23	12.4	98.3
HC.S10	51.5	10.4	2.44	11.4	2.7	5.14	1.44	0.72	0.10	0.46	0.10	0.16	12.8	99.3
HC.S12	51.1	11.5	3.3	10.7	2.1	5.92	1.65	0.42	0.06	0.30	0.11	0.14	12.2	99.5
HC.S15	50.4	11.6	4.2	9.46	2.9	4.48	2.1	0.69	0.05	0.32	0.10	0.13	12.6	99.0
HC.S23	51.5	10.6	3.86	10.7	1.8	5.93	1.52	0.48	0.07	0.48	0.07	0.25	12.8	100
HC.S25	51.4	10.8	2.82	10.2	2.20	5.77	2.34	0.60	0.02	0.35	0.08	0.12	12.5	99.2
HC.S29	51.8	10.6	2.80	9.65	1.90	4.10	1.54	0.42	0.05	4.87	0.14	0.26	12.3	100.4
HC.S31	50.4	10.6	3.60	10.5	1.14	5.32	1.32	0.25	0.07	2.82	0.08	0.14	12.4	98.7
HC.S33	51.2	9.70	2.76	10.6	1.11	4.63	1.46	0.27	0.02	6.71	0.06	0.21	11.5	100.3
HC.S37	49.9	9.60	2.44	10.8	2.08	5.18	1.77	0.3	0.04	5.70	0.07	0.33	11.6	99.8
HC.S42	50.3	10.7	2.75	10.6	2.10	4.46	1.93	0.46	0.06	5.82	0.06	0.12	11.1	100.4
T-C1	50.2	9.48	2.38	10.1	1.42	7.818	1.07	0.44	0.10	1.07	0.11	0.08	14.4	98.7
T-C2	49.7	9.97	3.04	9.41	1.11	7.63	2.04	0.48	0.11	2.16	0.15	0.25	13.9	100.1
T-C3	51.2	9.7	2.91	10.6	2.08	6.84	1.8	0.31	0.02	1.24	0.07	0.32	12.4	99.6
T-C4	51.3	9.85	3.26	10.7	2.03	6.10	1.61	0.40	0.02	2.72	0.15	0.16	11.5	99.8
T-C5	50.3	10.5	2.38	9.74	1.42	7.81	1.07	0.40	0.10	1.37	0.12	0.08	14.4	99.8
T-C6	47.7	9.92	3.04	11.4	1.11	7.63	2.04	0.48	0.11	1.4	0.15	0.25	13.9	99.2
T-C7	49.4	9.42	5.13	9.22	2.04	6.9	1.27	1.1	0.06	0.87	0.08	0.34	12.7	98.6
T-C8	49.6	10.1	5.74	8.98	2.02	6.84	2.41	0.97	0.02	0.63	0.09	0.29	13.3	101
T-C9	51.2	9.70	4.96	10.3	1.85	5.76	1.63	0.36	0.02	1.21	0.05	0.17	11.8	99.1
T-C10	49.9	9.60	5.83	9.87	2.11	5.25	1.52	0.34	0.04	0.70	0.07	0.23	13.2	98.6
T-C11	50.3	10.7	3.44	10.2	2.07	5.73	1.87	0.51	0.10	1.46	0.04	0.31	12.9	99.6
T-C12	50.7	11.4	4.73	10.3	2.40	4.75	1.35	0.39	0.11	0.74	0.08	0.22	12.4	99.6
T-C13	51.4	10.3	2.56	11.1	2.05	5.24	1.4	0.72	0.10	1.16	0.12	0.168	13.8	100.2
T-C14	51.7	10.4	2.79	10.6	2.32	5.65	2.26	0.60	0.02	0.65	0.11	0.14	12.4	99.8
T-C15	50.8	10.6	3.82	9.98	2.44	5.23	1.47	0.42	0.05	1.24	0.14	0.30	12.1	98.6
T-C16	50.7	10.8	2.88	10.6	2.16	4.79	1.83	0.46	0.06	1.73	0.07	0.17	13.3	99.7
T-C17	49.9	9.78	6.7	9.31	2.40	6.76	1.43	1.14	0.06	0.48	0.08	0.31	11.7	100
T-C18	49.4	10.4	6.62	9.63	2.48	6.58	1.26	0.75	0.14	0.83	0.17	0.10	12.4	100.8
T-C19	50.7	11.3	3.86	11.2	2.30	5.25	1.81	0.79	0.07	0.64	0.07	0.23	11.3	99.6
T-C20	51.5	10.4	2.44	11.3	2.60	4.68	1.37	0.72	0.12	1.46	0.10	0.16	13.1	100
T-C21	50.8	11.2	3.29	9.82	2.40	5.79	1.71	0.42	0.08	0.97	0.16	0.18	12.4	99.3
T-C22	50.2	10.7	4.52	9.44	1.85	5.17	1.56	0.42	0.11	1.76	0.14	0.25	13.8	100
T-C23	49.4	9.66	6.74	11.2	2.63	6.25	1.24	0.25	0.05	0.92	0.08	0.12	11.5	100.1
T-C24	51.7	9.75	3.46	9.87	1.94	6.77	1.82	0.46	0.02	1.20	0.12	0.22	12.6	100
T-C25	50.4	10.1	4.32	8.95	2.21	6.76	1.55	1.12	0.04	1.04	0.14	0.30	12.5	99.5
T-C26	49.8	10.3	5.86	10.7	2.38	4.77	1.39	0.40	0.04	1.87	0.09	0.25	12.3	100.2
T-C27	49.8	11.4	4.56	9.96	2.55	5.97	1.62	0.34	0.11	2.42	0.07	0.14	11.4	100.4
T-C28	48.3	10.8	6.04	10.4	1.72	5.85	1.80	0.51	0.1	0.96	0.04	0.34	11.9	98.7

Table 4
Representative EPMA analyses of pyrites from the Cheshmeh-Konan copper deposit in wt% (bdl: below detection limit).

No.	Minerals	Se	As	Ge	S	Pb	Bi	Sb	Sn	Fe	Co	Te	Ag	Cd	Zn	Cu	Ni	Au	Mn	Total
1	Framboidal pyrite	bdl	0.04	bdl	52.77	0.01	bdl	0.01	0.01	45.98	0.12	0.01	0.03	bdl	0.01	0.34	bdl	bdl	bdl	99.32
2	Framboidal pyrite	bdl	0.12	0.01	53.02	0.21	bdl	0.01	bdl	45.25	0.06	bdl	0.01	bdl	bdl	0.67	0.04	0.03	bdl	99.44
3	Framboidal pyrite	bdl	0.06	0.01	52.48	bdl	bdl	0.02	bdl	45.63	0.01	0.04	0.01	0.03	0.01	0.14	1.62	bdl	0.03	100.08
4	Framboidal pyrite	bdl	0.08	bdl	52.53	bdl	bdl	bdl	0.01	46.04	0.02	0.03	bdl	0.01	0.01	0.38	0.04	0.05	0.01	99.21
5	Framboidal pyrite	bdl	0.14	bdl	53.67	0.37	bdl	0.01	bdl	45.22	0.01	0.01	bdl	0.01	0.04	0.22	0.15	0.02	0.02	99.89
6	Framboidal pyrite	bdl	0.05	0.01	52.44	0.26	bdl	bdl	bdl	46.95	0.16	bdl	bdl	0.04	bdl	0.05	bdl	bdl	bdl	99.96
7	Framboidal pyrite	bdl	0.13	bdl	53.65	bdl	bdl	0.01	bdl	45.39	0.12	0.01	0.12	0.02	0.02	0.12	0.02	0.01	0.02	99.64
8	Framboidal pyrite	bdl	bdl	bdl	53.19	0.03	bdl	0.03	bdl	45.21	0.09	0.01	0.12	0.01	bdl	0.23	0.54	0.02	0.02	99.49
9	Fine grained Pyrite	bdl	0.04	bdl	52.58	0.14	bdl	bdl	bdl	45.41	0.14	0.02	0.14	0.02	0.02	0.75	0.25	0.02	0.03	99.56
10	Fine grained Pyrite	bdl	0.15	bdl	53.46	bdl	bdl	bdl	bdl	45.38	0.21	bdl	0.01	bdl	bdl	0.67	bdl	bdl	bdl	99.88
11	Fine grained Pyrite	bdl	0.10	bdl	52.21	1.25	bdl	0.01	bdl	43.95	0.10	bdl	0.08	0.03	0.02	2.54	0.02	0.01	bdl	100.32
12	Fine grained Pyrite	bdl	0.14	bdl	52.27	0.34	bdl	bdl	bdl	43.17	0.04	0.04	0.05	0.01	0.01	3.31	0.08	0.05	bdl	99.51
13	Fine grained Pyrite	bdl	0.09	bdl	53.39	0.47	bdl	bdl	bdl	44.61	0.16	bdl	0.01	0.01	0.03	0.85	0.01	bdl	bdl	99.63
14	Fine grained Pyrite	bdl	bdl	bdl	51.42	0.13	bdl	bdl	bdl	43.83	0.12	0.01	bdl	0.01	0.07	3.74	0.14	0.04	0.02	99.53
15	Fine grained Pyrite	bdl	0.12	0.01	51.87	0.44	bdl	0.04	bdl	45.72	0.05	0.04	0.26	0.02	0.02	0.94	0.02	bdl	0.03	99.57
16	Fine grained Pyrite	bdl	0.08	bdl	52.15	0.46	bdl	0.01	bdl	43.32	0.36	bdl	0.14	bdl	bdl	3.31	0.03	0.04	0.01	99.91
17	Fine grained Pyrite	bdl	0.17	bdl	52.89	0.52	bdl	bdl	bdl	44.39	0.09	bdl	bdl	bdl	0.05	1.65	0.01	0.07	0.02	99.87

able organic matter, and reactive Fe (Williams, 1978). The temporal sequence from early diagenetic pyrite to later addition of copper iron sulfides and later chalcocite is a common feature of the SSC deposits (Brown, 1984; Chartrand and Brown, 1985).

7.2. Source of sulfur

The range of δ³⁴S measured for Cheshmeh-Konan pyrites (−41.9 to −16.4‰) is consistent with a bacteriogenic derivation

Table 5

Representative EPMA analyses of chalcopyrite, bornite and chalcocite I from the Cheshmeh-Konan copper deposit in wt% (bdl: below detection limit).

No.	Minerals	Se	As	Ge	S	Pb	Bi	Sb	Sn	Fe	Co	Te	Ag	Cd	Zn	Cu	Ni	Au	Mn	Total
1	Chalcopyrite	bdl	0.23	bdl	34.32	bdl	bdl	bdl	0.01	31.62	0.03	bdl	0.01	0.01	bdl	33.72	bdl	0.02	bdl	99.97
2	Chalcopyrite	bdl	bdl	bdl	34.62	bdl	bdl	bdl	bdl	30.13	0.01	bdl	bdl	bdl	0.05	34.56	bdl	0.05	0.01	99.43
3	Chalcopyrite	bdl	0.03	bdl	34.32	0.21	bdl	0.01	0.04	30.79	0.01	bdl	bdl	bdl	bdl	33.87	bdl	bdl	bdl	99.28
4	Chalcopyrite	bdl	0.03	bdl	34.70	0.03	bdl	bdl	bdl	29.85	bdl	0.01	0.04	bdl	0.02	34.61	bdl	bdl	bdl	99.29
5	Chalcopyrite	bdl	0.12	bdl	34.93	bdl	bdl	bdl	bdl	29.86	bdl	bdl	0.01	bdl	bdl	34.57	bdl	0.03	bdl	99.52
6	Chalcopyrite	bdl	0.14	bdl	34.51	0.01	bdl	0.01	0.02	30.88	bdl	0.04	0.04	bdl	bdl	34.54	bdl	0.02	bdl	100.21
7	Chalcopyrite	bdl	0.21	0.01	34.74	bdl	bdl	bdl	bdl	29.83	0.01	bdl	0.02	0.03	0.07	34.49	bdl	0.12	bdl	99.53
8	Chalcopyrite	bdl	bdl	bdl	34.26	0.42	bdl	bdl	bdl	29.70	0.01	bdl	bdl	bdl	0.01	35.52	bdl	bdl	bdl	99.92
9	Chalcopyrite	bdl	bdl	bdl	34.87	bdl	0.01	bdl	0.03	29.86	bdl	0.01	0.06	bdl	bdl	34.64	bdl	0.02	0.02	99.52
10	Chalcopyrite	bdl	0.12	bdl	34.48	0.59	bdl	bdl	bdl	30.03	bdl	0.01	0.01	0.01	bdl	34.72	bdl	bdl	bdl	99.54
11	Chalcopyrite	bdl	0.24	0.01	34.53	0.07	bdl	0.01	0.04	29.64	0.01	bdl	bdl	bdl	0.03	34.68	bdl	0.09	bdl	99.36
12	Chalcopyrite	bdl	bdl	bdl	33.81	bdl	bdl	bdl	bdl	30.21	bdl	bdl	0.03	bdl	0.01	35.65	bdl	0.02	bdl	99.71
13	Bornite	bdl	0.17	bdl	31.26	bdl	bdl	bdl	bdl	13.36	0.01	bdl	0.06	bdl	bdl	54.68	bdl	bdl	bdl	99.54
14	Bornite	bdl	0.02	bdl	31.57	0.01	bdl	bdl	bdl	12.24	bdl	0.03	0.12	0.02	0.04	55.62	bdl	0.02	Bdl	99.69
15	Bornite	bdl	bdl	bdl	33.72	bdl	0.01	bdl	0.01	11.68	0.03	bdl	0.04	0.03	0.01	54.34	bdl	0.11	bdl	99.98
16	Bornite	bdl	bdl	bdl	31.61	bdl	bdl	bdl	bdl	12.16	bdl	bdl	0.10	bdl	bdl	55.45	bdl	bdl	bdl	99.32
17	Bornite	bdl	bdl	bdl	31.53	0.02	bdl	bdl	bdl	13.25	0.03	bdl	0.01	bdl	0.02	55.94	bdl	0.04	0.01	100.94
18	Bornite	bdl	0.12	bdl	31.25	0.11	bdl	0.02	0.04	13.54	0.01	bdl	0.04	0.02	0.03	54.15	bdl	bdl	bdl	99.33
19	Bornite	bdl	0.17	bdl	31.43	0.14	bdl	0.01	0.01	12.40	0.02	bdl	0.02	bdl	bdl	55.23	bdl	bdl	Bdl	99.43
20	Bornite	bdl	0.22	0.01	31.37	bdl	bdl	bdl	bdl	13.31	bdl	bdl	0.08	bdl	0.03	54.87	bdl	0.04	Bdl	99.94
21	Chalcocite I	bdl	bdl	bdl	20.83	bdl	bdl	bdl	bdl	0.03	bdl	bdl	0.38	bdl	0.06	78.76	bdl	bdl	Bdl	100.06
22	Chalcocite I	bdl	bdl	bdl	21.04	0.01	bdl	bdl	0.01	bdl	bdl	bdl	0.16	bdl	bdl	78.39	bdl	0.04	Bdl	99.67
23	Chalcocite I	bdl	0.11	0.01	21.09	0.01	bdl	bdl	bdl	0.01	0.02	bdl	0.07	0.02	0.04	78.82	bdl	0.02	0.12	100.34
24	Chalcocite I	bdl	bdl	bdl	21.17	bdl	bdl	0.01	0.03	0.04	bdl	bdl	0.72	0.01	0.11	77.75	bdl	bdl	bdl	99.84
25	Chalcocite I	bdl	0.03	bdl	21.78	bdl	bdl	bdl	bdl	0.02	bdl	bdl	0.65	0.04	0.04	77.24	bdl	0.01	0.02	99.83
26	Chalcocite I	bdl	0.16	bdl	21.30	0.02	bdl	bdl	bdl	0.01	bdl	bdl	0.18	bdl	0.03	77.97	bdl	bdl	bdl	99.67

Table 6

Representative EPMA analyses of chalcocite II and covellite from the Cheshmeh-Konan copper deposit in wt% (bdl: below detection limit).

No.	Minerals	Se	As	Ge	S	Pb	Bi	Sb	Sn	Fe	Co	Te	Ag	Cd	Zn	Cu	Ni	Au	Mn	Total
1	Chalcocite II	bdl	bdl	0.01	20.96	bdl	bdl	0.01	bdl	0.03	0.03	bdl	0.08	0.01	0.03	78.82	bdl	0.03	bdl	100.01
2	Chalcocite II	bdl	bdl	0.01	21.19	0.01	bdl	bdl	bdl	bdl	0.01	0.01	0.26	0.03	0.07	79.25	bdl	0.04	bdl	100.88
3	Chalcocite II	bdl	bdl	bdl	21.54	bdl	bdl	bdl	0.01	0.01	bdl	bdl	0.14	bdl	0.04	77.64	bdl	bdl	0.01	99.39
4	Chalcocite II	bdl	bdl	bdl	21.72	0.02	bdl	0.01	bdl	0.04	0.02	bdl	0.17	bdl	0.01	77.28	bdl	bdl	bdl	99.27
5	Chalcocite II	bdl	bdl	bdl	21.31	bdl	bdl	bdl	bdl	0.04	0.03	0.01	0.64	0.03	0.04	77.97	bdl	0.02	bdl	100.09
6	Chalcocite II	bdl	bdl	bdl	22.43	bdl	bdl	bdl	bdl	bdl	bdl	bdl	0.09	bdl	bdl	77.39	bdl	0.02	bdl	99.93
7	Chalcocite II	0.01	bdl	bdl	22.18	0.02	0.01	0.02	bdl	bdl	bdl	bdl	0.37	0.02	bdl	77.13	bdl	bdl	bdl	99.76
8	Chalcocite II	bdl	bdl	bdl	21.69	bdl	bdl	bdl	0.01	bdl	bdl	bdl	0.26	0.03	bdl	77.82	bdl	bdl	0.01	99.82
9	Chalcocite II	bdl	bdl	bdl	21.34	bdl	bdl	bdl	bdl	bdl	bdl	0.01	0.45	bdl	0.04	77.67	bdl	0.01	bdl	99.52
10	Covellite	bdl	bdl	bdl	21.72	bdl	bdl	bdl	bdl	0.04	0.03	bdl	0.68	bdl	0.02	76.92	bdl	bdl	bdl	99.41
11	Covellite	bdl	bdl	0.01	22.31	0.01	bdl	bdl	0.03	bdl	bdl	bdl	0.22	0.02	0.01	77.26	bdl	bdl	bdl	99.87
12	Covellite	bdl	bdl	bdl	22.67	0.02	0.01	0.01	bdl	bdl	bdl	bdl	0.44	0.02	0.01	76.56	bdl	0.02	bdl	99.76
13	Covellite	bdl	bdl	bdl	21.62	bdl	bdl	0.02	bdl	0.03	0.03	bdl	0.23	bdl	0.02	77.78	bdl	bdl	bdl	99.73
14	Covellite	bdl	bdl	bdl	21.25	bdl	bdl	bdl	0.02	0.01	bdl	0.01	0.94	bdl	bdl	77.92	bdl	0.03	bdl	100.18
15	Covellite	bdl	bdl	0.01	21.19	0.01	bdl	bdl	bdl	bdl	bdl	bdl	0.65	0.01	bdl	78.06	bdl	0.02	bdl	99.95
16	Covellite	bdl	bdl	bdl	21.43	bdl	bdl	bdl	bdl	bdl	bdl	bdl	1.21	bdl	bdl	77.24	bdl	bdl	0.01	99.89
17	Covellite	bdl	bdl	bdl	22.65	bdl	bdl	bdl	bdl	0.03	0.01	bdl	0.26	0.01	0.01	76.85	bdl	bdl	bdl	99.82

Table 7

A summary of fluid inclusion microthermometric data of quartz and calcite in the Cheshmeh-Konan copper deposit.

Sample	Mineral	n	Th (°C)			Tmi (°C)			Salinity (wt% CaCl₂ eq.)		
			max	avg	min	max	avg.	min	max	avg.	min
HC.S18	Quartz	23	141	132	125	−37.6	−38.5	−38	34	34	34
HC.S19	Quartz	26	160	151	140	−25.1	−25.6	−26	26	26	25
HC.S29	Calcite	20	139	133	128	−36.4	−36.5	−36.5	33	33	33
HC.S35	Quartz	21	152	147	137	−39.5	−40	−41.5	38	36	35
CR.S1	Calcite	33	109	104	96	−34.4	−35.5	−36	33	32	31
CR.S3	Quartz	27	155	148	142	−30	−30	−30	28	27	26

Key: n: number of analyzed inclusions, Th: temperature of homogenization, Tmi: temperature of ice melting (freezing point depression); min: minimum value; avg: average; max: maximum value.

of the sulfur (Ohmoto and Rye, 1979), with reduction occurring at first in an environment closed to sulfate exchange and low temperatures, i.e. in a sulfate-limited environment. Petrographic and sulfur isotope evidence indicates two different sources of sulfur for the Cu-sulfides in the Cheshmeh-Konan deposit: (1) locally from pyrite replacement and (2) from an external source. Thus, horizons containing abundant diagenetic pyrite would be able to produce copper mineralization, replacement being the dominant process of Cu-sulfide generation. In such a case, both sulfide sulfur and organic carbon were consumed during interac-

Table 8

C–O isotopic data for calcite and dolomite associated with Cu–mineralization and sulfur isotopic compositions of pyrites and Cu-sulfides in the Cheshmeh-Konan copper deposit.

Sample No.	Mineral	$\delta^{18}O_{V-PDB}$ (‰)	$\delta^{13}C_{V-PDB}$ (‰)	$\delta^{34}S_{CDT}$ (‰)
HC.S1	Calcite	−7.89	−7.23	
HC.S4	Calcite	−9.83	−7.52	
HC.S7	Calcite	−7.72	−5.85	
HC.S17	Calcite	−9.43	−5.85	
HC.S3	Dolomite	−9.76	−7.11	
HC.S11	Dolomite	−8.22	−6.23	
HC.S14	Dolomite	−7.18	−5.11	
HC.S16	Dolomite	−8.87	−7.52	
HC.S18	Dolomite	−10.21	−8.2	
HC. S35	Dolomite	−10.33	−6.68	
HC.S1	Framboidal Pyrite			−37.9
HC.S4	Framboidal Pyrite			−38.6
HC.S16	Framboidal Pyrite			−35.8
HC.S7	Fine-grained Pyrite			−29.2
HC.S11	Fine-grained Pyrite			−27.6
HC.S18	Fine-grained Pyrite			−16.4
HC.S1	Chalcopyrite			−11.3
HC.S3	Chalcopyrite			−9.0
HC.S14	Chalcopyrite			−12.0
HC.S6	Bornite			−10.4
HC.S11	Bornite			−13.1
HC.S17	Chalcocite			−14.6
HC. S35	Chalcocite			−12.6
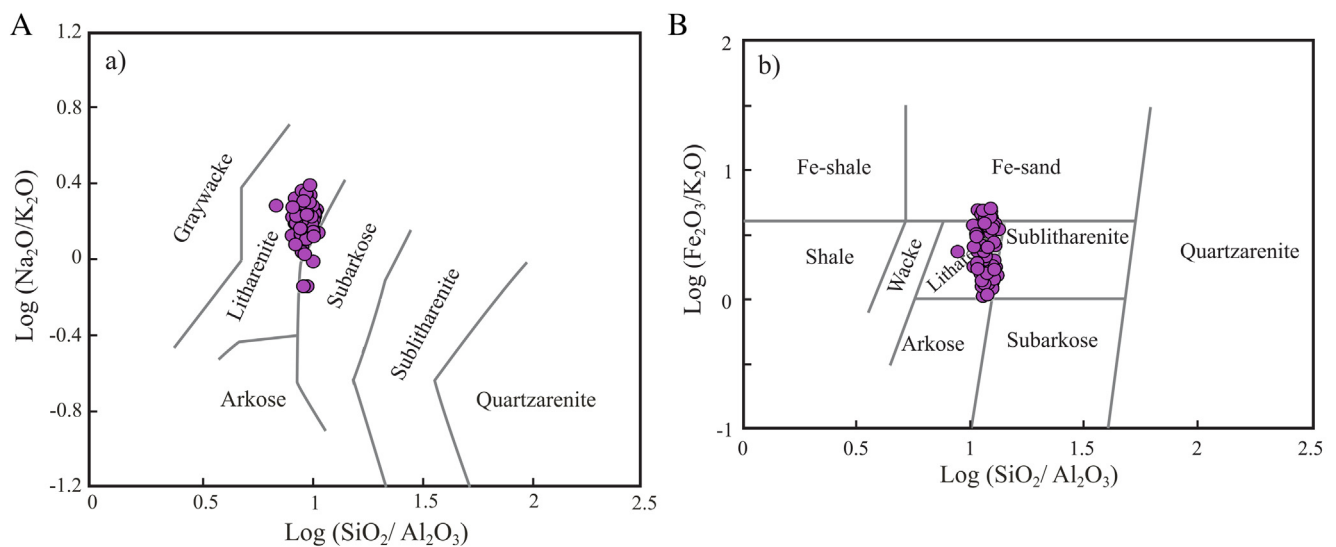
Fig. 10. Chemical classification of the Cheshmeh-Konan sandstone samples based on (a) log (SiO₂/Al₂O₃) vs. log (Na₂O/K₂O) diagram of Pettijohn et al. (1972); (b) log (SiO₂/Al₂O₃) vs. log (Fe₂O₃/K₂O) diagram of Herron (1988).

tion between reduced sediments and an oxidized Cu-bearing fluid.

Chalcopyrite, bornite and chalcocite show distinctly heavier sulfur isotope compositions than pyrite, with $\delta^{34}S$ values ranging from −14.6 to −9.0‰, and there are no obvious distinctions between the isotopic compositions of the various ore-stage Cu-sulfide minerals. Because the Cu-sulfides generally show features of replacement of pyrite, these sulfides could be expected to have sulfur isotopic compositions resembling those of the replaced pyrite, which is not the case. Therefore, it is likely that additional sulfur was introduced to the sediments during the mineralization process, i.e. bacterial reduction of sulfate-bearing basinal brines, as is the case in many SSC deposits (Haynes, 1986; Burnie et al., 1972; Branam and Ripley, 1990).

7.3. Source of carbon

The carbon and oxygen isotopes of carbonates can be used to trace the source of carbon in the ore-forming fluids (Ohmoto and Rye, 1979; Branam and Ripley, 1990). Zheng et al. (2006) pointed out that the $\delta^{13}C$ values of methane vary from light to heavy along with the increase of the thermal evolution of coal-measure source rocks. In other words, the lighter isotopes are released preferentially, and they likely dissolved into pore fluids to provide a lighter carbon isotope composition of the carbonate cement. The low $\delta^{13}C$ values of carbonate cement imply the limited addition of organic carbon. During diagenesis of the host sandstone, disseminated anhedral and subhedral pyrite was formed by extensive bacterial reduction of sulfate with concomitant oxidation of organic matter, and by hydrolysis reactions of organic matter that produced CH_4 and CO_2 (Shikazono and Utada, 1997). The major reason responsible for these diagenetic events is that, along with increasing burial depth, the temperature and pressure gradually increased to boost decarboxylation of organic matter and released carbon dioxide with lighter carbon ($\delta^{13}C$ values usually range from −4.0 to −35.0‰) (Suess and Whiticar, 1989).

The $\delta^{13}C_{V-PDB}$ versus $\delta^{18}O_{V-PDB}$ plot of bulk calcite and dolomite cements in the Cheshmeh-Konan deposit shows a positive correla-
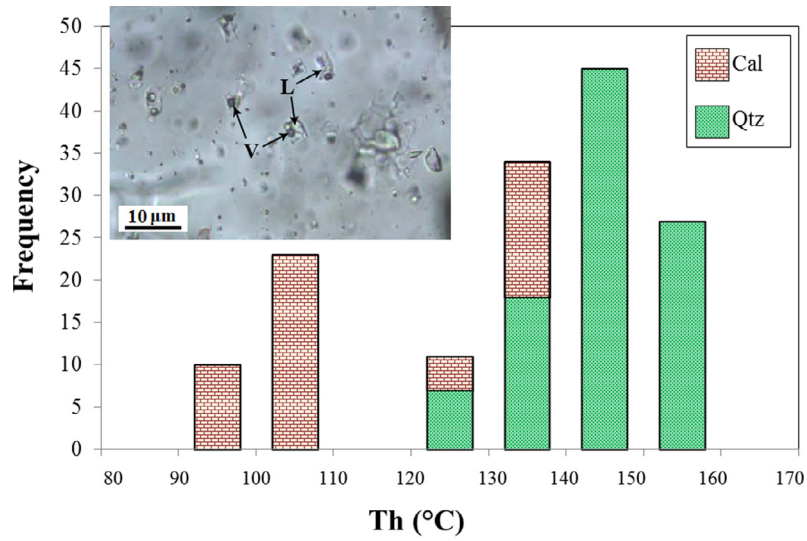
Fig. 11. Histograms of homogenization temperature and of salinity in equiv. wt% $CaCl_2$ of primary fluid inclusions in calcite and quartz from the Cheshmeh-Konan copper deposit. The top-left inset shows a photomicrograph of representative primary, liquid-vapor fluid inclusions in quartz of the mineralized sandstones.
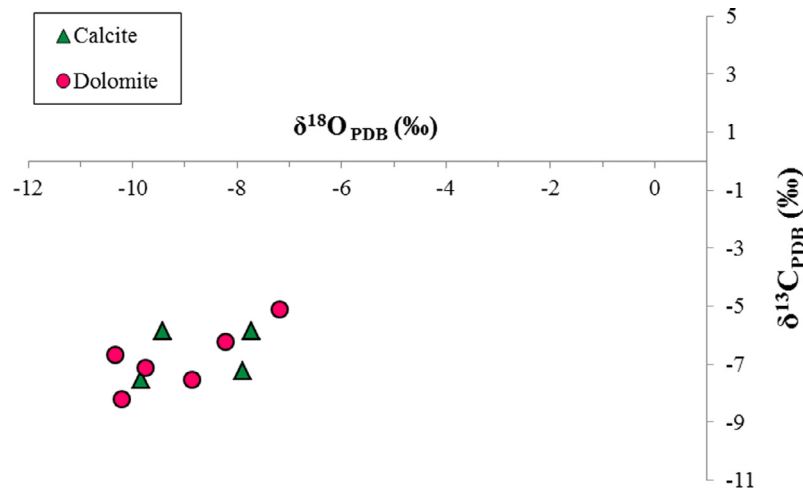
Fig. 12. $\delta^{13}C_{V-PDB}$ (‰) versus $\delta^{18}O_{V-PDB}$ (‰) plot of bulk calcite and dolomite cements showing a positive correlation.
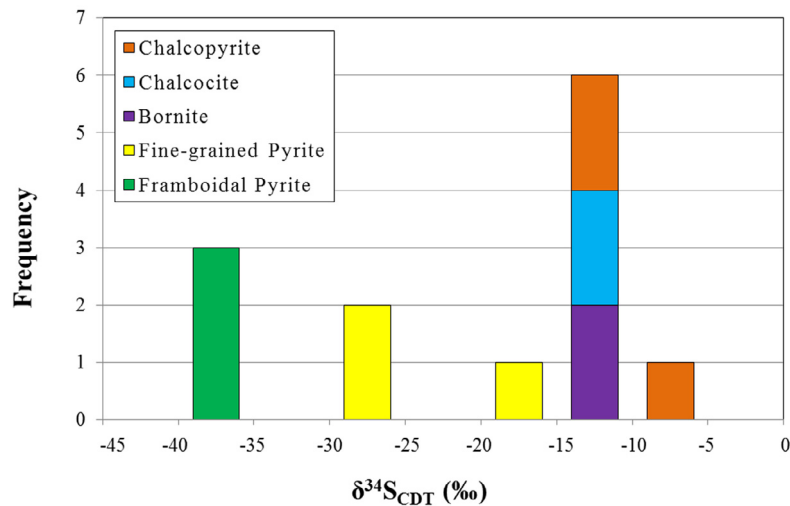
Fig. 13. Histograms showing the distribution of $\delta^{34}S$ values of pyrites and copper sulfides in the Cheshmeh-Konan copper deposit.

tion, which is attributed to an increasing input in ^{12}C from thermal alteration of organic matter during progressive burial diagenesis and increasing temperature (Fig. 12). The $\delta^{13}C_{V\text{-}PDB}$ values of dolomite (−8.2 to −5.1‰) suggest that dissolved carbon was derived from multiple sources, such as thermal alteration of organic matter and from the dissolution of cogenetic carbonate cements (Fig. 12; Irwin et al., 1977; Surdam et al., 1984).

The carbon isotope data look typical of early diagenetic cements in which part of the carbon comes from oxidation of organic carbon (ca. −20‰) and the rest from HCO_3^- from seawater (ca. +0‰) in a proportion of about 2:1 of seawater: organic matter. Once formed, carbonate minerals do not exchange C, but they readily exchange O, so the $\delta^{18}O$ signal is from meteoric water or it could be late diagenetic water at higher temperatures because the calcite and dolomite compositions are identical. A simple way to interpret the C−O isotope correlation in this case is burial diagenesis with high fluid/rock ratio (Marshall, 1992; Melim et al., 2004; Knauth and Kennedy, 2009; Preto et al., 2009). While no primary depositional processes have been identified that can produce the correlated $\delta^{18}O$–$\delta^{13}C$ arrays, simulations show that fluid–rock interaction with high pCO_2 fluids is capable of producing such arrays at geologically reasonable pCO_2 and water–rock ratios. Variations in the Mg/Ca ratio of the fluid phase determine the extent of dolomite vs. calcite in the resulting mineral assemblage. The negative $\delta^{13}C$ values can be adequately explained by diagenetic processes. Diagenetic alteration can produce correlated $\delta^{18}O$–$\delta^{13}C$ arrays in carbonates via several mechanisms. Correlations recognized over large scales can result from differences in the temperature of fluid–rock interaction (Seewald, 2003). Arrays can result from either mixing of carbonate formed in different environments (Swart, 2008) or carbonate formed from mixtures of different fluids (Melim et al., 2004). The data imply $\delta^{13}C$ values of dissolved CO_2 are low in many basinal and meteoric fluids because of the contribution from oxidation of sedimentary organic matter. Fluids with different chemical and isotopic compositions can mix and react with host rocks, resulting in the replacement or precipitation of carbonates with a wide range of isotopic values.

It is characteristic of dolomites that formed in a marine environment during sedimentation and early diagenesis to be partly or completely recrystallized and depleted in $\delta^{18}O$ and/or $\delta^{13}C$ during burial fluid flow (e.g., Smith and Dorobek, 1993; Nielsen et al., 1994; Hitzman and Beaty, 1996). According to Machel et al. (1995), the authigenic carbonates that form as by-products of bacterial sulfide reduction can obtain their carbon from two principal sources: very light organic carbon released from oxidation of organic matter or hydrocarbons and inorganic carbon, with a marine $\delta^{13}C$ signature. The carbonates in samples within or close to the mineralization have isotopically light values ($\delta^{13}C_{V\text{-}PDB}$ = −8.2 to −5.1‰ and $\delta^{18}O_{V\text{-}PDB}$ = −10.3 to −7.2‰). It is suggested that metal deposition was mainly controlled by reduction–oxidation reac-

tions, i.e., former organic matter (evidenced by low $\delta^{13}C$ values) facilitated reduction of sulfate to H_2S, resulting in copper sulfide precipitation.

7.4. Source of metals

According to EPMA results, framboidal pyrite has low concentrations of Cu and Ag compared to the fine-grained pyrite, implying that the depositional environment was not enriched in these elements in the Cheshmeh-Konan copper deposit. However, these elements are considerably enriched in later hydrothermal fluids as demonstrated by their contents in fine-grained pyrite that formed during syn- to early-diagenesis stages. The trace element content of pyrite is considered to reflect the composition of the fluids from which the pyrite formed, which accounts for the heterogeneity in the trace element contents between the two pyrite generations (Berner et al., 2013). The content of Au, Ag, Pb, Co, As, Zn and Cu increases whereas the content of Ni and Sn decreases from synsedimentary framboidal pyrite to diagenetic fine-grained pyrite, and also the content of As and Sb slightly increases in late pyrite. The geochemical data indicate that the Cheshmeh-Konan deposit has locally a relatively high silver content in the Cu-rich sulfides (supergene chalcocite II up to 0.27 wt% Ag and covellite up to 0.40 wt% Ag). The EPMA results for copper sulfide minerals show copper is preferentially enriched in supergene covellite, and this mineral is the major Ag-carrier. No inclusions of Ag minerals were detected in the microprobe work. Intense supergene overprint not only formed enrichment in copper, but also in silver. According to Fig. 14, the relationship between Ag and other base metals in the whole-rock of mineralized samples in the Cheshmeh-Konan deposit indicates that the distribution of Ag in the ores has a relatively strong correlation with Cu (r = 0.75), while the correlation with Pb (r = 0.25) and Zn (r = 0.34) is less pronounced.

7.5. Source of ore-forming fluid

The fluid inclusion microthermometry on quartz and calcite indicates that the copper mineralization is related to a diagenetic fluid with a moderate-to-low temperature (Th = 96–160 °C) but high salinity (25–38 wt% $CaCl_2$ equiv.). The regional geological setting of the Cheshmeh-Konan deposit is consistent with its assignment to the sandstone-hosted copper deposit class (i.e., SSC type). The Cheshmeh-Konan mineralization is hosted by a major continental redbed system, in combination with evaporitic rocks and locally reducing lithologies (Brown, 1984, 1992, 1997; Jowett, 1989; Kirkham, 1989, 1995; Hitzman et al., 2005, 2010). This setting assures that large amounts of copper may have been leached by oxic brines from the molasse-style redbed sedimentation and the volcanic arc materials, and concentrated at redox traps such as organic material and synsedimentary/diagenetic pyrite.
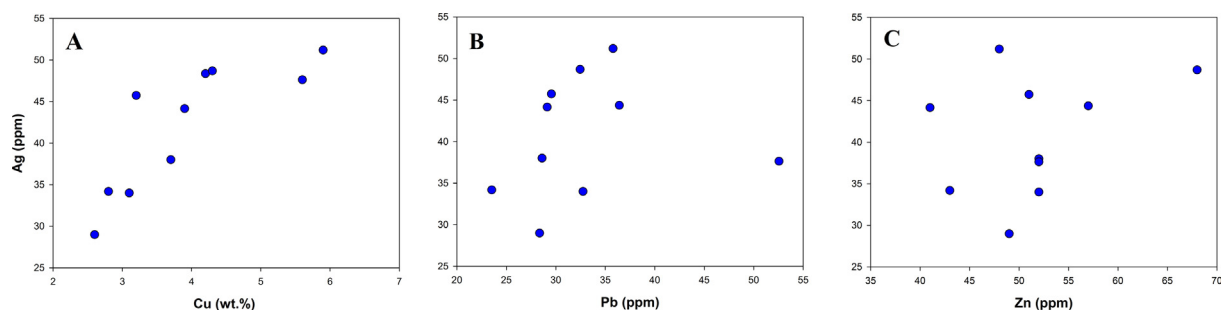

Fig. 14. Ag versus Cu, Pb, and Zn contents in the mineralized whole-rock samples in the Cheshmeh-Konan copper deposit.

8. Conclusions

Petrographic and microthermometric data indicate that the Cheshmeh-Konan deposit formed epigenetically after the blockage of primary permeability by carbonate cementation in the Red Bed Formation. Copper sulfides occur primarily as replacements of diagenetic pyrite, which, in turn, replaced organic matter; that is, mineralization occurred during diagenesis. Overprint by cupriferous fluids formed Cu-bearing sulfides by replacement of pyrite. The metal deposition was mainly controlled by reduction–oxidation reactions, i.e., former organic matter (evidenced by low $\delta^{13}C$ values) facilitated reduction of sulfate to H_2S, resulting in copper sulfide precipitation. The main mineralization controls include grain size (permeability), content of organic matter, the amount and degree of feldspar and calcite dissolution and the presence of NW–SE trending faults.

Sulfur likely was added to the ore-forming system via sulfate reduction of basinal brines, with organic matter providing a direct source of the reducing potential. Petrographical studies show that in the mineralized zones, copper mineralization took place primarily as chalcopyrite, then bornite and chalcocite, respectively, as replacement. Subsequently, subrecent weathering produced supergene enrichment with chalcocite, covellite and malachite.

EPMA results indicate that the syn-sedimentary framboidal pyrite has low concentrations of Cu and Ag. Successive generations of fine-grained pyrite formed as a consequence of authigenic and diagenetic processes. High copper content (up to 3.74 wt%) in fine-grained pyrite could be related to submicroscopic inclusions of Cu-bearing mineral phases, such as chalcopyrite and/or bornite, and indicates that pyrite is replaced by Cu-sulfide phases. Our study shows that the trace metal composition of pyrite can be used as an indicator of the ore generation and for variations in fluid composition, which helps to understand the genesis of sedimentary copper deposits. During supergene enrichment, copper and silver are reprecipitated in chalcocite and covellite. The high concentration of silver in covellite reveals that this element was accumulated during weathering.

The fluid inclusion microthermometry on authigenic quartz and calcite indicates that the Cu mineralization is related to a diagenetic fluid phase with a moderate-to-low temperature (Th = 96–160 °C) but high salinity (25–38 wt% $CaCl_2$ equiv.). The fluid migration away from fault planes into the sandstone was likely enhanced by the presence of fractures and micro-cracks. Late diagenetic and relatively recent oxidation processes overprinted the orebodies enhancing copper and silver grades.

Acknowledgments

References

Aghazadeh, M., Badrzadeh, Z., 2011. Sediment hosted Cu mineralization periods in Iran. In: Conference paper, Twenty-Ninth Meeting Geological Sciences, Geological Survey of Iran, 11 pp.

Aghazadeh, M., Badrzadeh, Z., 2012. Sediment-hosted Cu mineralization in Iran: main metallogenic basins and mineralization periods. Abstr. 34th International Geological Congress, Australia.

Aghazadeh, M., Prelevic, D., Badrzadeh, Z., Braschi, E., Bogaard, P., Conticelli, S., 2015. Geochemistry, Sr–Nd–Pb isotopes and geochronology of amphibole- and mica-bearing lamprophyres in northwestern Iran: implications for mantle wedge heterogeneity in a palaeo-subduction zone. Lithos 216–217, 352–369.

Amini, A., 1997. Provenance and Depositional Environment of the Upper Red Formation, Central Zone, Iran (Ph.D. thesis). University of Manchester.

Amini, A., Anketell, J.M., 2015. Textural and geochemical studies of detrital Fe–Ti oxides and test of their validity in provenance determination, a case study from Central Iran. J. Afr. Earth Sc. 103, 140–152.

Annels, A.E., 1974. Some aspects of the stratiform ore deposits of the Zambian copper belt and their genetic significance. In: Bartholomé, P. (Ed.), Gisements Stratiformes Et Provinces Cuprifères. Soc. Géol Belgique, Liège, pp. 235–254.

Baas Becking, L.G.M., Kaplan, I.R., Moore, D., 1960. Limits of the natural environment in terms of pH and oxidation-reduction potentials. J. Geol. 68, 243–284.

Berberian, M., King, G.C., 1981. Towards a paleogeography and tectonic evolution of Iran. Can. J. Earth Sci. 18, 210–265.

Berberian, M., 1983. Continental deformation in the Iranian plateau. Geological Survey of Iran, Report No. 52, 626 pp.

Berner, R.A., 1970. Sedimentary pyrite formation. Am. J. Sci. 268, 1–23.

Berner, R.A., 1984. Sedimentary pyrite formation: an update. Geochim. Cosmochim. Acta 48, 605–615.

Berner, Z., Puchelt, H., Nöltner, T., Kramer, U., 2013. Pyrite geochemistry in the Toarcian Posidonia Shale of south-west Germany: evidence for contrasting trace-element patterns of diagenetic and syngenetic pyrites. Sedimentology 60, 548–573.

Boyle, R.W., Brown, A.C., Jefferson, C.W., Jowett, E.C., Kirkham, R.V., (Eds.), 1989. Sediment-Hosted Stratiform Copper Deposits. Geological Association of Canada, Special Paper 36, pp. 1–710.

Branam, T.D., Ripley, E.M., 1990. Genesis of sediment-hosted copper mineralization in south-central Kansas: sulfur/carbon and sulfur isotope systematics. Econ. Geol. 85, 601–621.

Brookfield, M.E., 1977. The emplacement of giant ophiolite nappes: I. Mesozoic-Cenozoic examples. Tectonophysics 37, 247–303.

Brown, A.C., 1971. Zoning in the White Pine copper deposit, Ontonogan County, Michigan. Econ. Geol. 66, 543–573.

Brown, A.C., 1984. Alternative sources of metals for stratiform copper deposits. Precambr. Res. 25, 61–74.

Brown, A.C., 1992. Sediment-hosted stratiform copper deposits. Geosci. Canada 19, 125–141.

Brown, A.C., 1997. World-class sediment-hosted stratiform copper deposits: characteristics, genetic concepts and metallotects. Aust. J. Earth Sci. 44, 317–328.

Brown, A.C., 2009. A process-based approach to estimating the copper derived from red beds in the sediment-hosted stratiform copper deposit model. Econ. Geol. 104, 857–868.

Burnie, S.W., Schwartz, H.P., Crockett, J.H., 1972. A sulfur isotopic study of the White Pine mine, Michigan. Econ. Geol. 67, 895–914.

Chartrand, F.M., Brown, A.C., 1985. The diagenetic origin of stratiform copper mineralization, Coates Lake, Redstone Belt, NWT, Canada. Econ. Geol. 80, 325–343.

Crawford, M.L., 1981. Phase equilibria in aqueous fluid solutions. Mineralogical Association of Canada, Short Course Series 6, 75–100.

Davis, D.W., Lowenstein, T.K., Spencer, R.J., 1990. The melting behavior of fluid inclusions in laboratory-grown halite crystals in the systems NaCl-H_2O, NaCl-KCl-H_2O, NaCl-$MgCl_2$-H_2O and NaCl-$CaCl_2$-H_2O. Geochim. Cosmochim. Acta 54, 591–601.

Dewey, J.F., Pitman, W.C., Ryan, W.B.F., Bonnin, J., 1973. Plate tectonic and evolution of the Alpine system. Geol. Soc. Am. Bull. 84, 3137–3180.

Einaudi, M.T., 1968. Copper zoning in pyrite from Cerro de Pasco. Peru. Am. Mineral. 53, 1748–1752.

Fallick, A., McConville, P., Boyce, A.J., Burgess, R., Kelley, S.P., 1992. Laser microprobe stable isotope measurements on geological materials: some experimental considerations (with special reference to $\delta^{34}S$ in sulfides). Chem. Geol. 101, 53–61.

Farhoudi, G.A., 1978. Comparison of Zagros geology to island arcs. J. Geol. 86, 323–334.

Folk, R.L., 1980. Petrology of Sedimentary Rocks. Hemphill's Book Store, Austin, Texas, p. 185.

Foster, H., 1976. Continental drift in Iran in relation to the Afar structures. In: Pilger, A., Rosler, E. (Eds.), Afar Between Continental and Oceanic Rifting, vol. II. Schweizerbartsche Verlagsbuchhandlung, Stuuttgart, pp. 182–190.

Ghorashi, M., Arshadi, S., 1978. 1:250000 Geological Map of Khoy published by Geological Survey of Iran, Tehran.

GSI, 1999. Geological Map of Iran published by Geological Survey of Iran (GSI), Tehran.

Haynes, D.W., 1986. Stratiform copper deposits hosted by low energy sediments: I. Timing of sulfide precipitation–an hypothesis. Econ. Geol. 81, 250–265.

Herron, M.M., 1988. Geochemical classification of terrigenous sands and shales from core or log data. J. Sediment. Petrol. 58, 820–829.

Hitzman, M.W., Beaty, D.W., 1996. The Irish Zn-Pb-(Ba) orefield. In: Sangster, D.F. (Ed.), Carbonate-Hosted Lead-Zinc Deposits, Society of Economic Geologists, vol. 4. Spec. Publ., pp. 112–143.

Hitzman, M.W., Kirkham, R., Broughton, D., Thorson, J., Selley, D., 2005. The sediment-hosted stratiform copper ore system. Econ. Geol. 100th Anniversary Volume, 609–642.

Hitzman, M.W., Selley, D., Bull, S., 2010. Formation of sedimentary rock-hosted stratiform copper deposits through Earth history. Econ. Geol. 105, 627–639.

Huston, D.L., Sie, S.H., Suter, G.F., Cooke, D.R., Both, R.A., 1995. Trace elements in sulfide minerals from eastern Australian volcanic-hosted massive sulfide deposits: part I, proton microprobe analyses of pyrite, chalcopyrite, and

sphalerite, and part II, selenium levels in pyrite: comparison with δ^{34}S values and implications for the source of sulfur in volcanogenic hydrothermal systems. Econ. Geol. 90, 1167–1196.

Irwin, H., Curtis, C., Coleman, M., 1977. Isotopic evidence for source of diagenetic carbonates formed during burial of organic rich sediments. Nature 269, 209–213.

Jowett, E.C., 1989. Effects of continental rifting on location and genesis of stratiform copper–silver deposits. In: Boyle, R.W., Brown, A.C., Jefferson, C.W., Jowett, E.C., Kirkham, R.V., (Eds.), Sediment-Hosted Stratiform Copper Deposits. Geological Association of Canada, Special Paper 36, pp. 53–66.

Jung, D., Kürsten, M., Tarakian, M., 1976. Post-Mezozoic volcanism in Iran and its relation to the subduction of Afro-Arabian plate under the Eurasian Plate. In: Pilger, A., Rösler, E. (Eds.), Afar Between Continental and Oceanic Rifting, vol. II. Schweizerbartsche Verlagsbuchhandlung, Stuttgart, pp. 175–181.

Kelley, S.P., Fallick, A.E., 1990. A high precision spatially resolved analysis of δ^{34}S in sulfides using a laser extraction technique. Geochim. Cosmochim. Acta 54, 883–888.

Khodabandeh, A.A., Aminifazl, A., 1993. 1:100000 Geological Map of Tasuj published by Geological Survey of Iran (GSI), Tehran.

Kirkham, R.V., 1989. Distribution, setting and genesis of sediment hosted stratiform copper deposits. In: Boyle, R.W., Brown, A.C., Jefferson, C.W., Jowett, E.C., Kirkham R.V., (Eds.), Sediment-Hosted Stratiform Copper Deposits. Geological Association of Canada, Special Paper 36, pp. 3–38.

Kirkham, R.V., 1995. Sediment-hosted stratiform copper. In: Eckstrand, O.R., Sinclair, W.D., Thorpe, R.I., (Eds.), Geology of Canadian Mineral Deposit Types. Geological Survey of Canada 8, pp. 223–240.

Knauth, L.P., Kennedy, M.J., 2009. The late Precambrian greening of the Earth. Nature 460, 728–732.

Machel, H.G., Krouse, H.R., Sassen, R., 1995. Products and distinguishing criteria of bacterial and thermochemical sulfate reduction. Appl. Geochem. 10, 373–389.

Marshall, J.D., 1992. Climatic and oceanographic isotopic signals from the carbonate rock record and their preservation. Geol. Mag. 129, 143–160.

Melim, L.A., Swart, P.K., Eberli, G.P., 2004. Mixing-zone diagenesis in the subsurface of Florida and the Bahamas. J. Sediment. Res. 74, 904–913.

Naghizadeh, R., Shiva, A., Dori, M., Riazi, N., 2008. Survey of sedimentary copper mineralization in Tasuj, East Azerbaijan province. In: Conference paper, 26th Conference of Geological Society of Iran, 6 pp.

Nielsen, P., Swennen, R., Keppens, E., 1994. Multiple-step recrystallization within massive ancient dolomite units: an example from the Dinantian of Belgium. Sedimentology 41, 567–584.

Nowroozi, A.A., 1971. Seismo-tectonics of the Persian Plateau, Eastern Turkey, Caucasus and Hindu-Kush regions. Bull. Seismol. Soc. Am. 61, 317–341.

Ohmoto, H., Rye, R., 1979. Isotopes of sulfur and carbon. In: Barnes, H.L. (Ed.), Geochemistry of Hydrothermal Ore Deposits. second ed. Wiley, New York, pp. 509–567.

Pacevski, A., Libowitzky, E., Zivkovic, P., Dimitrijevic, R., Cvetkovic, L., 2008. Copper-bearing pyrite from the Coka Marin polymetallic deposit, Serbia: mineral inclusions or true solid-solution? Can. Mineral. 46, 249–261.

Pettijohn, F.J., Potter, P.E., Silver, R., 1972. Sand and Sandstone. Springer, New York, p. 618.

Preto, N., Spotl, C., Guaiumi, C., 2009. Evaluation of bulk carbonate delta C-13 data from Triassic hemipelagites and the initial composition of carbonate mud. Sedimentology 56, 1329–1345.

Rahimpour-Bonab, H., Kalantarzadeh, Z., 2005. Origin of the secondary potash deposits; a case from Miocene evaporites of NW central Iran. J. Asian Earth Sci. 25, 157–166.

Rahimpour-Bonab, H., Shariatinia, Z., Siemann, M.G., 2007. Origin and geochemistry of Miocene marine evaporites associated with red beds: Great Kavir Basin, Central Iran. Geol. J. 42, 37–54.

Rajabpour, S., Alipour, S., Abedini, A., Zakeri, L., 2010a. Petrography and geochemistry of the upper red beds sandstones in Cheshmeh-Konan of Tasuj. Implications for tectonic setting and conditions of source rock weathering. In: Conference paper, 28th Conference of Geological Society of Iran, 6 pp.

Rajabpour, S., Abedini, A., Alipour, S., Zakeri, L., 2010b. Investigation of mineralization and genesis of stratiform copper in Cheshmeh-Konan area of Tasuj. East-Azarbaidjan Province. In: Conference paper, 28th Conference of Geological Society of Iran, 6 pp.

Rajabpour, S., Abedini, A., Alipour, S., Zakeri, L., 2013. Investigation of mineralization and genesis of stratiform copper in Cheshmeh-Konan area of Tasuj, East-Azarbaijan province. J. Econ. Geol. 5, 49–63 (in Persian).

Reich, M., Deditius, A., Chryssoulis, S., Wei Li, J., Qiang Ma, C., Parada, M.A., Barra, F., Mittermayr, F., 2013. Pyrite as a record of hydrothermal fluid evolution in a porphyry copper system: a SIMS/EMPA trace element study. Geochim. Cosmochim. Acta 104, 42–62.

Roedder, E., 1984. Fluid Inclusions. Reviews in Mineralogy 12, 644 p.

Sadati, N., Yazdi, M., Behzadi, M., Adabi, M.H., Mokhtari, A.A., 2013. The role of organic matter in genesis of sedimentary-hosted stratiform copper deposits in Nahand-Ivand area, NW Iran. In: Goldschmidt Conference Abstracts, p. 211.

Sadati, N., Yazdi, M., Mao, J., Behzadi, M., Adabi, M.H., Lingang, X., Zhenyu, C., Mokhtari, A.A., 2016. Sulfide mineral chemistry investigation of sediment-hosted stratiform copper deposits, Nahand-Ivand area, NW Iran. Ore Geol. Rev. 72, 760–776.

Seewald, J.S., 2003. Organic–inorganic interactions in petroleum-producing sedimentary basins. Nature 426, 327–333.

Shikazono, N., Utada, M., 1997. Stable isotope geochemistry and diagenetic mineralization associated with the Tono sandstone-type uranium deposit in Japan. Miner. Deposita 32, 596–606.

Smith, T.M., Dorobek, S.L., 1993. Alteration of early-formed dolomite during shallow to deep burial: mississippian Mission Canyon Formation, central to southwestern Montana. Geol. Soc. Am. Bull. 105, 1389–1399.

Suess, E., Whiticar, M.J., 1989. Methane-derived CO_2 in pore fluids expelled from the Oregon subduction zone. Palaeogeogr. Palaeoclimatol. Palaeoecol. 71, 119–136.

Surdam, R.C., Boese, S.W., Crossey, L.J., 1984. The chemistry of secondary porosity. In: McDonald, D.A., Surdam, R.C. (Eds.), Clastic Diagenesis. American Association of Petroleum Geologists, Memoir 37, pp. 127–149.

Swart, P.K., 2008. Global synchronous changes in the carbon isotopic composition of carbonate sediments unrelated to changes in the global carbon cycle. Proc. Natl. Acad. Sci. U.S.A. 105, 13741–13745.

Sweeney, M.A., Turner, P., Vaughan, D.J., 1986. Stable isotope and geochemical studies of the role of early diagenesis in ore formation, Konkola Basin, Zambian Copperbelt. Econ. Geol. 81, 1836–1852.

Williams, N., 1978. Studies of the base metal sulfide deposits at McArthur River, Northern Territory, Australia: II. The sulfide-S and organic-C relationships of the concordant deposits and their significance. Econ. Geol. 73, 1036–1056.

Zheng, J., Hu, H., Sun, G., Ji, L., 2006. Carbon isotopic characteristics of hydrocarbon gases from coal-measure source rock, a thermal simulation experiment. Chin. J. Geochem. 25, 167–172.